Simulation of African Easterly Waves in a Global Climate Model

XIANAN JIANG[a,b] HUI SU[a,c] SHUYI S. CHEN[d] AND PAUL A. ULLRICH[e]

[a] *Joint Institute for Regional Earth System Science and Engineering, University of California, Los Angeles, California*
[b] *Jet Propulsion Laboratory, California Institute of Technology, Pasadena, California*
[c] *Department of Atmospheric and Oceanic Sciences, University of California, Los Angeles, California*
[d] *Department of Atmospheric Sciences, University of Washington, Seattle, Washington*
[e] *Department of Land, Air, and Water Resources, University of California, Davis, Davis, California*

(Manuscript received 15 February 2022, in final form 11 September 2022)

ABSTRACT: African easterly waves (AEWs) exert significant influence on local and downstream high-impact weather including tropical cyclone (TC) genesis over the Atlantic. Accurate representation of AEWs in climate and weather prediction models therefore is necessary for skillful predictions. In this study, we examine simulated AEWs, including their evolution, vertical structure, and linkage to tropical cyclone genesis, in the NASA Goddard Earth Observing System Model, version 5 (GEOS-5) atmospheric global climate model. Identified by the leading empirical orthogonal function mode of time-filtered precipitation, the observed westward propagating AEWs along the southern track over the Atlantic are largely captured in GEOS-5, but with a slower phase speed and significantly weaker amplitude downstream off the West Africa coast. The weak downstream development of AEWs in GEOS-5 is accompanied by much reduced TC genesis over the main development region. Further analyses suggest that the slow westward propagation and weaker AEW amplitude downstream can be ascribed to a weak African easterly jet, while overestimated negative (positive) meridional potential vorticity (PV) gradients appear to the north (south) of 10°N in GEOS-5. The greatly overestimated positive meridional PV gradient to the south of 10°N is expected to generate strong horizontal stretching in the AEW wave pattern in the model, which hinders organization of convection and its feedback to sustain the AEW development. Persistent and vigorous AEW precipitation in the Guinea Highlands of the West Africa coast could also be responsible for reduced westward propagation of AEWs in the model.

KEYWORDS: Synoptic climatology; Hurricanes/typhoons; General circulation models; Tropical variability

1. Introduction

Originating over eastern and central Africa with westward propagation across West Africa and the Atlantic, African easterly waves (AEWs) have been identified as the primary synoptic-scale disturbances with prominent influence over tropical Africa and the Atlantic during boreal summer, as reported by several pioneering works (Carlson 1969; Frank 1970; Burpee 1974). For example, AEWs strongly modulate mesoscale convective systems (MCS) over Africa (Machado et al. 1993; Fink and Reiner 2003; Kiladis et al. 2006; Laing et al. 2008; Tomassini 2018; Russell et al. 2020) and associated extreme rainfall events (Duvel 1990; Diedhiou et al. 1999; Gu et al. 2004; Crétat et al. 2015; Lafore et al. 2017). AEWs also strongly interact with equatorial waves, including the convectively coupled Kelvin and Rossby waves (Ventrice et al. 2012a; Mounier et al. 2007; Ventrice et al. 2011; Mekonnen et al. 2006, 2008; Yang et al. 2018; Mantripragada et al. 2021) and with the Madden–Julian oscillation (Mounier et al. 2008; Lavender and Matthews 2009; Ventrice et al. 2011; Alaka and Maloney 2012), and may even have a cross-scale influence on the intraseasonal (Sultan et al. 2003) and interannual (Grist 2002) variability of the west African monsoon rainfall. AEWs are attributed in a majority of tropical cyclone genesis events over the Atlantic basin (Landsea and Gray 1992; Landsea 1993; Avila et al. 2000; Thorncroft and Hodges 2001; Russell et al. 2017). Improved understanding and modeling capability of AEWs, therefore, is critical for skillful climate and weather prediction in this region.

Numerous observational and modeling studies have explored key processes regulating AEWs. In general, it has been widely recognized that AEWs are generated by dynamical instability of the large-scale environment over Africa (Charney and Stern 1962). Specifically, due to the reversal of the meridional gradient of background potential vorticity (PV) associated with wind shear of the African easterly jet (AEJ), and as a result of the strong meridional gradient of low-level temperature to the south of the Sahara Desert, AEWs can be energized through a combination of barotropic and baroclinic energy conversions from the mean atmospheric environment (Burpee 1972; Rennick 1976; Norquist et al. 1977; Albignat and Reed 1980; Thorncroft and Hoskins 1994; Dickinson and Molinari 2000). This traditional view that AEWs are dynamically driven, however, has been questioned in recent studies that emphasize a critical role of moist convection in triggering and sustaining AEWs. On one hand, it was suggested that the reversal of the PV gradient can be more closely associated with convective heating over the Atlantic intertropical convergence zone (ITCZ) than the strength of horizontal and vertical wind shear associated with

Su's current affiliation: Department of Civil and Environmental Engineering, the Hong Kong University of Science and Technology, Hong Kong, China.

Corresponding author: Xianan Jiang, xianan@ucla.edu

DOI: 10.1175/JCLI-D-22-0090.1

the AEJ (e.g., Schubert et al. 1991; Hsieh and Cook 2005, 2008). On the other hand, the coupling between convection and AEWs itself can represent an important energy or PV source for growth of AEWs (e.g., Berry and Thorncroft 2005; Hsieh and Cook 2007; Janiga and Thorncroft 2014; Grogan et al. 2016; Tomassini et al. 2017; Russell et al. 2020). The critical role of convective heating in sustaining AEWs is also supported by idealized modeling studies showing that finite-amplitude upstream precursors seem to be essential for realistic simulations of AEWs (e.g., Hall et al. 2006; Thorncroft et al. 2008).

Despite recent progress in studies of AEWs, significant gaps remain toward full understanding of key processes governing AEW activity, including the relative role of diabatic heating and dynamical instability for genesis and growth of AEWs. Meanwhile, our present-day global climate models (GCMs) also exhibit large biases in representing AEW propagation and maintenance. A large spread of AEW activity over West Africa and the Atlantic was found across the models in phase 3 of the Coupled Model Intercomparison Project (CMIP3), which tends to be closely linked to model biases in seasonal mean West African monsoon precipitation and TC genesis in the main development region (MDR) over the Atlantic (e.g., Daloz et al. 2012; Skinner and Diffenbaugh 2013). These CMIP3 model simulations further suggest that skillful simulations of AEWs will require realistic depiction of convective wave coupling by the convective parameterization scheme, and energetic contributions by the large-scale circulation (Skinner and Diffenbaugh 2013). The importance of model cumulus parameterization for realistic AEW simulations is supported by the work of McCrary et al. (2014), which shows significant improvement of AEWs in the Community Climate System Model by replacing the conventional cloud parameterization with a two-dimensional cloud-resolving model. While large model biases in representing AEW activity still exist in CMIP5 models, another common bias of CMIP5 models is found that model AEWs are unable to propagate across the west Africa coast and into the Atlantic, which could be further associated with model biases in simulating convection over the Guinea Highlands (Martin and Thorncroft 2015; Brannan and Martin 2019). On the other hand, our predictive skill for AEWs also remains limited in state-of-the-art operational prediction systems (e.g., Torn 2010; Elless and Torn 2018).

In this study, the characteristics of simulated AEWs from a global climate model are examined so as to provide insights into important processes for realistic simulations of AEWs. A novel feature of this study is our focus on convective signals associated with AEWs in recent high-resolution satellite rainfall observations. These data effectively capture AEW activity over the Atlantic along the southern track around 10°N (e.g., Reed et al. 1988; Kiladis et al. 2006), a pathway that has been found to be closely linked to TC genesis over the MDR (e.g., Chen et al. 2008; Hopsch et al. 2007; Russell et al. 2017). Also, while previous modeling studies on AEWs mainly focused on eddy kinetic energy (EKE) or tracking (e.g., Martin and Thorncroft 2015; Brannan and Martin 2019; Bercos-Hickey and Patricola 2021), we focus on analyzing the detailed evolution and structures of AEWs in the model. A potential linkage between model deficiencies in AEWs and TC genesis over the Atlantic is also explored, although with some controversial opinions that will be discussed. The outline of this paper is as follows. In section 2, the observational datasets and climate model simulations used for this study, as well as the approach to identify AEWs are introduced. The main results from this study are presented in section 3, including comparison of summer mean state over the Atlantic-African sector, TC genesis, evolution characteristics, and vertical structure of AEWs between model simulations and observations. Possible processes responsible for model deficiencies in simulating AEWs are further discussed in section 3. A summary and discussion are presented in section 4.

2. Observational and model datasets

a. *Observational dataset*

The rainfall observations from the Global Precipitation Measurement (GPM) mission, the Integrated Multi-satellitE Retrievals for GPM (IMERG) is used to identify AEWs. The IMERG version 6 provides a global precipitation product by unifying observations from a network of partner satellites in the GPM constellation (Huffman et al. 2019). It provides high-resolution half-hourly precipitation estimates gridded at a 0.1° spatial resolution since 2000. In this study, 3-hourly averaged GPM rainfall observations are used to identify AEWs.

The latest high-resolution ERA5 reanalysis from the ECMWF (Hersbach et al. 2020) is analyzed to characterize the structure of AEWs and to serve as a benchmark for model simulations. ERA5 was produced using 4D-Var data assimilation in CY41R2 of the ECMWF's Integrated Forecast System, with a horizontal resolution of approximately 30 km at hourly time intervals, and 137 hybrid sigma/pressure model levels in the vertical and the top level at 0.01 hPa. Variables analyzed in this study include 6-hourly interpolated 3D variables (winds, vertical velocity, moisture, temperature, PV) at 27 pressure levels between 1000 and 100 hPa.

To account for uncertainties in temperature and specific humidity in ERA5 reanalysis, these two fields from satellite observations by the Atmospheric Infrared Sounder (AIRS, version 7; Chahine et al. 2006) are also analyzed. These AIRS observations are based on the Level-3 standard products at 12 pressure levels from 1000 to 100 hPa with 1° × 1° horizontal grid spacing. Note that AIRS observations are only available twice daily around 0130 and 1330 local time, corresponding to its descending and ascending orbits, respectively.

To explore a linkage between TC genesis and AEW activity, the observational TC data from the International Best Track Archive for Climate Stewardship (IBTrACS, version v04r00; Knapp et al. 2010) are also used, which provides 6-hourly TC location and maximum wind speed. The observed cyclogenesis locations are identified based on the IBTrACS best track at the time when the cyclone reaches tropical storm status (with wind speed $\geq$ 17.5 m s^{-1}) following previous studies (e.g., Jiang et al. 2018).

b. *NASA GEOS-5 global climate model simulations*

The model dataset analyzed in this study is based on the Atmospheric Model Intercomparison Project (AMIP)-type

simulations from the NASA Goddard Earth Observing System Model version 5 (GEOS-5) atmospheric GCM (AGCM), forced by historical sea surface temperature (SST) and sea ice during the period of 1980–2017 as a part of the MERRA-2 AMIP Project (Collow et al. 2017). The GEOS-5 AGCM uses the relaxed Arakawa–Schubert convection parameterization scheme with consideration of the re-evaporation of falling rain (Moorthi and Suarez 1992; Bacmeister et al. 2006), and with a stochastic Tokioka trigger function to govern the lower limits on the entrainment following Bacmeister and Stephens (2011). The prognostic cloud cover and cloud water and ice scheme is based on Bacmeister et al. (2006), and the turbulence is parameterized following the nonlocal scheme of Lock et al. (2000). Detailed model physics of GEOS-5 AGCM can be found in Molod et al. (2015). The simulations were performed using a c180L72 configuration of the cubed-sphere grid, with output fields archived on 0.5° latitude × 0.625° longitude grids. In this study, 3-hourly precipitation and 6-hourly sea level pressure (SLP), and 3D winds, vertical pressure velocity, specific humidity, PV, and temperature fields for the period of 2000–17 from GEOS-5 simulations are analyzed.

TCs in GEOS-5 simulations are detected based on the TempestExtremes algorithm (Ullrich and Zarzycki 2017; Zarzycki and Ullrich 2017; Ullrich et al. 2021), which mainly uses SLP as the feature-tracking variable. Geopotential height difference between 250 and 500 hPa is also used to constrain the warm core of TC in the upper troposphere. Locations of TC genesis based on GEOS-5 simulations during each summer are also defined when TC maximum wind speed reaches the tropical storm criterion as in the observations (i.e., >17.5 m s^{-1}).

In the following, analyses will be focused on the boreal summer season from July to September when AEWs are most active for the period of 2000–17 for both observations and model simulations. For analyses associated with AEWs, all the observational and model data are interpolated onto a common 1.5° × 1.5° grid. To extract variability in various fields associated with AEWs, these variables are subject to 2–6-day bandpass filtering (Duchon 1979) after removal of their corresponding climatological annual cycle (annual mean plus the three leading annual harmonics).

c. *Identification of AEWs based on empirical orthogonal functions*

In this analysis, AEWs in both observations and GEOS-5 simulations are identified by the leading modes from the empirical orthogonal function (EOF) analyses of 3-hourly 2–6-day bandpass-filtered GPM and model rainfall anomalies from July–September over the Atlantic sector (40°W–10°E; 0°–20°N). A similar EOF approach has been previously used for extracting the tropical depression-type waves over the western Pacific (e.g., Lau and Lau 1990; Zhao et al. 2016; Jiang et al. 2018) and for AEWs based on brightness temperature T_b (Cheng et al. 2019). Different from many previous studies (e.g., Cheng et al. 2019), in this study we did not apply the westward wavenumber–frequency filtering for 2–6-day rainfall anomalies prior to the EOF analyses to retain important multiscale convective features of AEWs, such as modulations of AEW convection over the Guinea Highlands to be discussed later. Instead, extraction of the dominant westward propagating AEW modes is achieved by the EOF analysis. For both observations and model simulations, the first two leading EOF modes represent the westward propagating AEWs with a 90° phase difference (refer to Fig. 5; details to be discussed). The first two leading modes together explain about 8.9% and 8.5% of total variances of 2–6-day filtered 3-hourly rainfall anomalies in observations and model simulation,[1] respectively, and are well separated from the rest of EOF modes based on North et al.'s (1982) criterion (not shown). The first principal component (PC_1) is then used as the AEW index to derive the evolution patterns as well as 3D structures associated with AEWs using the lag-regression approach for both observations and simulations. Using PC_2 or a combination of PC_1 and PC_2 yield very similar results although with a lag of about 1 day (~1/4 cycle) in the time evolution map when using PC_2 (figure not shown).

3. Results

a. *Summer mean state over the Atlantic-African sector*

Figure 1 illustrates summer mean precipitation and winds at 925 hPa in observations and GEOS-5 simulations. Over the Atlantic and African sectors, the most prominent features in summer mean precipitation in observations include the elongated Atlantic intertropical convergence zone (ITCZ) rainfall belt near 10°N, and its eastward extension connecting with a large area of rainfall over African continent. The two maximum centers of mean precipitation over the West Africa coast, one near the equatorial Gulf of Guinea and the other over the Guinea coast near 10°N, representing the two core regions of the western African monsoon (WAM). The northward shift of the ITCZ about the equator is associated with convergence of northeasterly and southeasterly trade winds to the north and south of the equator. Particularly, enhanced precipitation of the WAM is associated with low-level southwesterly winds connecting with the crossing-equatorial trade winds from the south.

The Atlantic ITCZ and WAM mean precipitation patterns, as well as the low-level circulation, including the trades winds and southwesterly monsoon flow over the West Africa coast, are well simulated in GEOS-5 (Fig. 1b), although several deficiencies are noted. For example, strong precipitation along the ITCZ extends farther west toward South America in

[1] The explained variances by the leading modes of AEWs in both observations and model in this study are smaller compared to that reported (about 16%) in previous studies (e.g., Cheng et al. 2019). This can be due to several differences: 1) T_b data at a horizontal resolution of 2.5° were used in Cheng et al. (2019), whereas 1.5° rainfall data are used in this study, which exhibits stronger spatial and temporal variations. 2) A wavenumber–frequency filtering was applied to extract the westward propagating wave component before the EOF analysis in Cheng et al. (2019), but not in this study. 3) A large domain (60°W–50°E, 30°N–30°S) was used for the EOF analysis in Cheng et al. (2019), while the analysis domain has a smaller coverage (40°W–10°E, 0°–20°N) in this study.

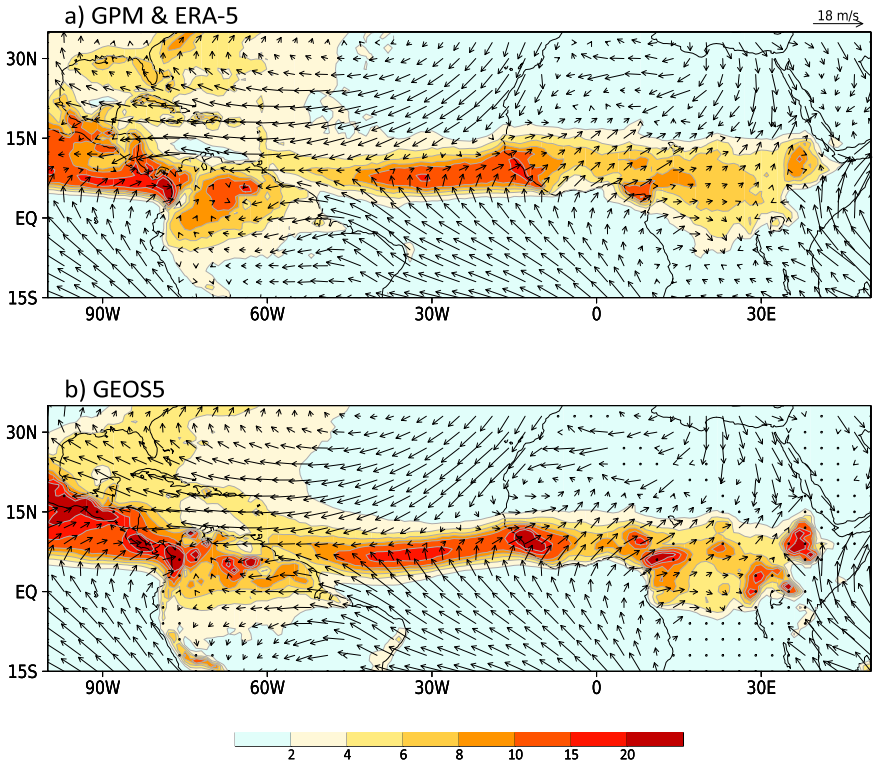

FIG. 1. Summer (July–September) mean precipitation (shaded with the color bar; mm day^{-1}) and winds at 925 hPa (vectors; see scale at the upper right) based on (a) observations (GPM and ERA5) and (b) GEOS-5 simulations.

GEOS-5 simulations than the observations, forming a strong precipitation center to the west of 30°W. Meanwhile, the WAM precipitation is much stronger than observations, particularly over the Guinea coast. In contrast to the maximum precipitation over the ocean off the Guinea in the observations (Fig. 1a), the maximum precipitation occurs over the land near the coast in the GEOS-5 simulations (Fig. 1b). This bias could be associated with the model representation of local orographic effects on precipitation over the Guinea Highlands due to limited resolution and cumulus parameterization in the model (e.g., Martin and Thorncroft 2015). Mean rainfall over the mountainous regions over central and East Africa is also overestimated in GEOS-5.

Figure 2 further presents vertical–latitudinal cross sections of summer mean meridional–vertical circulation (vectors) along with the zonal wind (shading) averaged over the Atlantic sector between 45°W and 10°E. The overturning Hadley cells are readily seen in the observations (Fig. 2a) with the ascending branch over the ITCZ region between 5° and 10°N, and descending over both sides of the equator. The convergence of low-level meridional winds toward the ITCZ region is associated with divergent flow in the upper troposphere near 200 hPa. The most prominent features of zonal wind in the lower troposphere include the westerly wind below 750 hPa between 5° and 10°N associated with the WAM as previously discussed, and the AEJ near 650 hPa and 15°N. The formation of the lower-tropospheric AEJ is generally ascribed to the strong northward temperature gradient over North Africa due to the presence of the Sahara Desert (to be discussed in Fig. 11e), despite recent debate that the diabatic heating over the ITCZ region possibly plays a more important role for the AEJ (e.g., Schubert et al. 1991; Hsieh and Cook 2005, 2008). As discussed in many previous studies, the configuration of low-level westerlies below 750 hPa and strong easterly wind near 650 hPa creates a unique environment for growth and maintenance of AEWs through a mixed baroclinic-barotropic instability due to a reversal of the meridional PV gradient (Charney and Stern 1962). In the upper troposphere, easterlies prevail over the tropical region while westerlies are evident in the extratropics over both hemispheres.

While these observed vertical–latitudinal circulation structures are reasonably simulated in GEOS-5, several model deficiencies are notable. For example, in the upper troposphere, the maximum equatorial easterlies appear above 150 hPa between 10° and 20°N (Fig. 2b) in GEOS-5 whereas they are observed near 200 hPa between 0° and 10°N (Fig. 2a); meanwhile, the observed westerly jet near 200 hPa and 30°N (Fig. 2a) is significantly underestimated in simulations (Fig. 2b). In the lower troposphere, both the low-level westerly winds associated with the WAM below 750 hPa and the AEJ near 650 hPa between 10° and 20°N are slightly weaker than their observed counterparts. As previously reported (e.g., Hall et al. 2006) and also to be discussed later, these subtle changes in the mean circulation could lead to significant influences on the AEW characteristics.

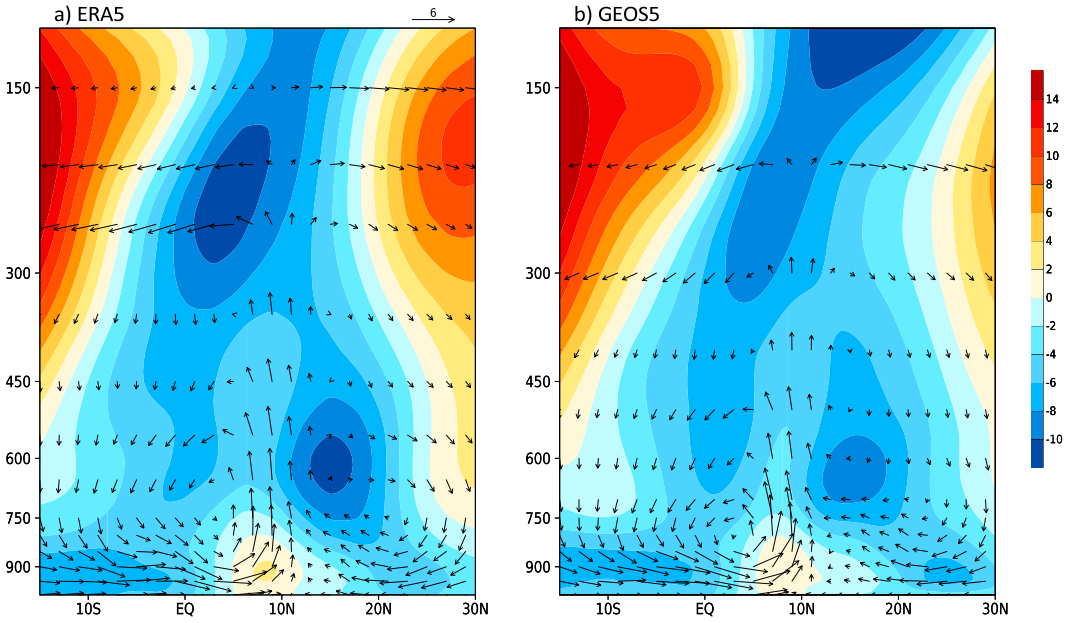

FIG. 2. Vertical–latitudinal cross sections of summer mean u-wind component (shaded with the color bar on the right; m s^{-1}) and meridional and vertical winds [vectors; see the scale above (a); m s^{-1} for v wind and 50 Pa s^{-1} for vertical p velocity; note that the sign of vertical p velocity is reversed] averaged over the Atlantic longitudinal bands of 45°W–10°E based on (a) ERA5 and (b) GEOS-5 simulations.

b. *Synoptic-scale variability and TC genesis*

Synoptic-scale variability associated with convection in observations is represented by standard deviations of 3-hourly 2–6-day filtered GPM precipitation anomalies (Fig. 3a). The strongest synoptic rainfall variability is found over the Atlantic ITCZ region off the West Africa coast and along a northwestward pathway toward the Caribbean Sea and the Bahamas, consistent with the typical tracks of westward propagating AEWs. Notably, in contrast to the narrow mean precipitation belt along the ITCZ in Fig. 1a, the rainfall variability exhibits a much broader pattern with strong variability over the northern edge of the ITCZ, indicating a significant influence of transient AEWs as previously reported (e.g., Kiladis et al. 2006). In stark contrast to the observations, strong synoptic-scale rainfall variability is confined over the narrow Atlantic ITCZ region and several mountainous areas over the African continent in the GEOS-5 simulations (Fig. 3b). The synoptic-scale convective variability in the model is largely suppressed over the Caribbean Sea and Bahamas. It is worth noting that very strong synoptic-scale variability is found over the eastern Pacific in GEOS-5 simulations, which is comparable to the observations and indicative that synoptic-scale variability over the eastern Pacific could be independent of the westward propagating AEWs crossing the Caribbean Sea.

Figure 4 further illustrates standard deviations of 2–6-day filtered meridional-wind anomalies at 900 hPa in both observations and GEOS-5 simulations. Very similar to previous studies based on the distribution of eddy kinetic energy (EKE; Martin and Thorncroft 2015), two maximum centers in synoptic-scale variability of circulations are found, one over West Africa along 20°N and another close to the Atlantic ITCZ, in accord with the north and south tracks of AEW activity as previously reported (e.g., Reed et al. 1988; Pytharoulis and Thorncroft 1999). The superimposed tropical storm genesis locations observed during the summers of 2000–17 clearly indicate frequent cyclogenesis over the MDR, collocated with synoptic wave activity along the AEW south track (Fig. 4a), and in agreement with many previous studies (Thorncroft and Hodges 2001; Chen et al. 2008; Martin and Thorncroft 2015; Dieng et al. 2017). A large number of cyclogenesis cases are also observed downstream over the Caribbean Sea and the Bahamas along the path of AEW propagation, suggesting a possibly important seeding effect of AEWs on Atlantic TC genesis.

In GEOS-5 simulations, while synoptic wave activity over the north track near 20°N is generally well captured, the observed strong activity center along the south track is largely absent in the model. Correspondingly, many fewer TC genesis events over the Atlantic basin than the observations are simulated in GEOS-5; in particular, very few TC genesis events are evident over the eastern part of the basin along the observed AEW south track. Many fewer TCs over the Atlantic basin in GEOS-5 AMIP simulations were also recently reported by Aarons et al. (2021), which is partially ascribed to the inability of the model grid to fully resolve detailed TC structure. Results from this study, as shown in Fig. 4, indicate that the lack of the seeding effect from AEWs on TC genesis could be associated with the suppressed TC activity in this model. However, it remains controversial whether the climatology of TC genesis over the Atlantic is controlled by the seeding effect from weather disturbances such as the AEWs (e.g., Patricola et al. 2018; Emanuel 2022). For example,

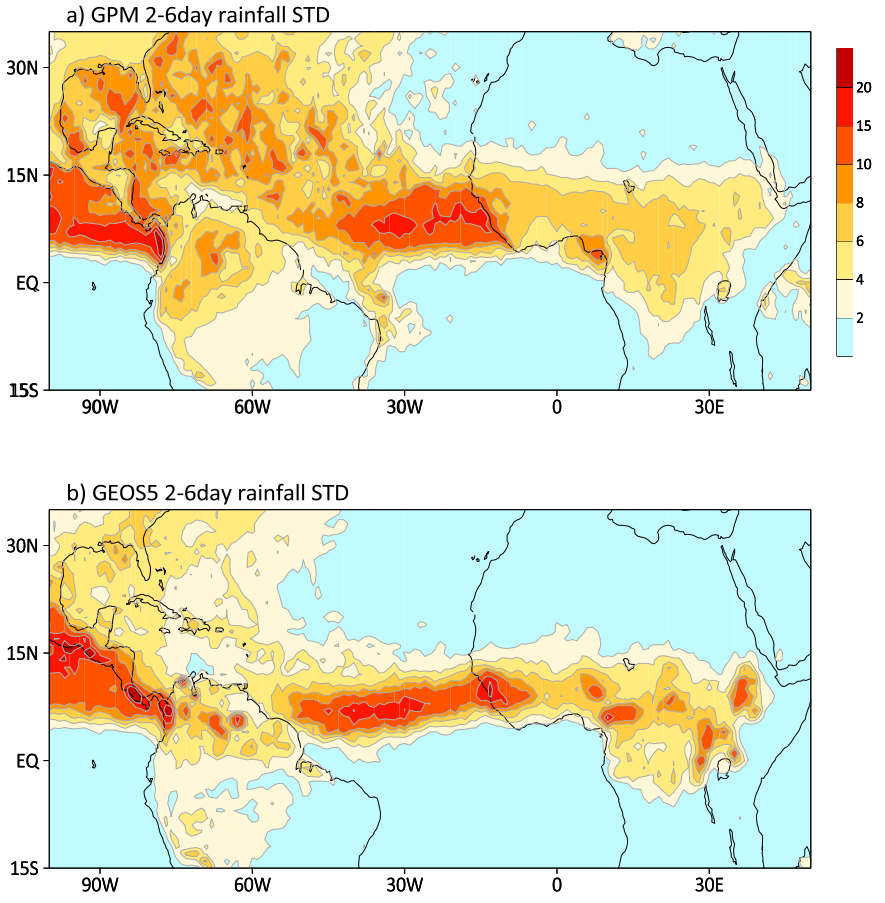

FIG. 3. Standard deviations of 2–6-day filtered 3-hourly precipitation anomalies during July–September (see color bar on the right; mm day^{-1}) based on (a) GPM observations and (b) GEOS-5 simulations.

recent modeling studies suggested that TC climatology tends to be insensitive to the characteristics of synoptic-scale disturbances (Patricola et al. 2018). Therefore, it is possible that suppressed AEW and TC activity in GEOS-5 simulations can be independent from each other, and both of them are due to model biases in the large-scale environment. Investigation of the role of AEW activity for climatological TC genesis over the Atlantic is beyond the scope of this study.

c. *Evolution characteristics of AEWs*

Evolution patterns of rainfall and 650-hPa relative vorticity anomalies associated with AEWs in the observations and GEOS-5 simulations are presented in Fig. 5. As previously mentioned, AEWs are identified as the leading EOF modes of 3-hourly 2–6-day filtered rainfall over the Atlantic sector. The evolution patterns shown in Fig. 5 are derived based on lag regression of 2–6-day filtered rainfall and vorticity anomalies on the corresponding PC_1 for observations and simulations. Note that although 3-hourly precipitation is used to identify AEWs, the regression analyses in this section are conducted on 6-hourly data for both observations and models, unless noted otherwise. In the observations (Fig. 5a), enhanced AEW convection anomalies first appear over the coastal region near the Gulf of Guinea, associated with the positive vorticity anomalies to the south of convection (day −1.5; Fig. 5a). Convection over West Africa then migrates westward and amplifies, and become largely in phase with positive vorticity anomalies at day −0.5. Subsequently, enhanced (suppressed) convection is strongly coupled with positive (negative) vorticity, and propagates westward along the south track away from the West African coast. While convective signals are mainly confined over the ITCZ region to the south of 10°N, vorticity anomalies display a larger extension, particularly to the north of convection. When the waves propagate beyond 10°N to the west of 30°W, vorticity anomalies tend to be decoupled with convection. As a result, a southeast–northwest wave train pattern is evident in the vorticity field, while precipitation anomalies largely exhibit an east–west dipole pattern. As will be shown later, the vorticity anomalies associated with AEWs largely exhibit a barotropic structure in the lower to middle troposphere. Therefore, these vertically extended vorticity anomalies over the south track region can effectively modulate TC genesis (e.g., Emanuel and Nolan 2004), in accord with observed frequent cyclogenesis over the MDR

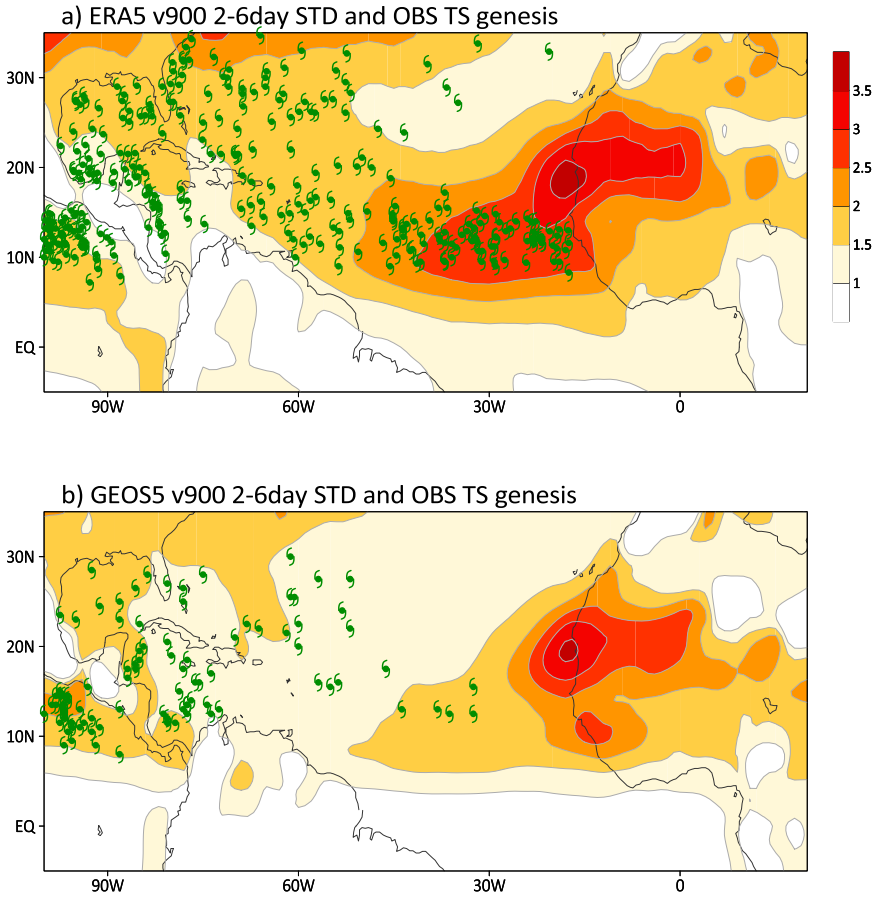

FIG. 4. Standard deviations of 2–6-day filtered 6-hourly v-wind anomalies at 900 hPa (shaded with the color bar on the right; m s^{-1}) along with locations of tropical storm genesis during 2000–17 summers based on (a) observations (ERA5 and the IBTrACS best track) and (b) GEOS-5 simulations. The TempestExtremes feature tracking algorithm following Ullrich et al. (2021) is used to detect tropical storms in GEOS-5 simulations.

(Fig. 4a). Moreover, a northeast–southwest tilt in both convection and vorticity anomalies is evident, indicating a role of the barotropic energy conversion in sustaining AEWs over this region.

Note that the leading AEW mode identified by GPM precipitation in Fig. 5a largely represents convective signals over the Atlantic and West African coast along the AEW south track. This result is different from the AEW pattern derived based on an EOF analysis of T_b in Cheng et al. (2019), which identified east–west-oriented AEW convection signals along 10°N with the origins of AEWs near the mountains over central and eastern Africa (their Fig. 3). Also, the circulation associated with AEWs tends to be much more widely extended in Cheng et al. (2019) than that shown in Fig. 5a. We hypothesize that T_b signals could be more closely associated with the high-cloud variability instead of surface precipitation as illustrated in this study.

Using the same lag-regression approach, evolution of AEWs simulated in GEOS-5 is illustrated in Fig. 5b. In contrast to largely smooth northwestward propagation of AEWs after departure from the West Africa coast in the observations, the model simulated AEW pattern exhibits a strong horizontal stretching with the anomalous vorticity pattern displaying a very narrow and nearly east–west oriented band. While the westward propagation of the main wave pattern is still discernible, they display a more north–south tilt compared to the observations (see the dashed lines at day 0 in Figs. 5a,b), and the westward propagation is mainly confined to the east of 30°W. Moreover, in contrast to significant enhancement of AEW convection over the ocean when moving off the Guinea coast in the observations, strong AEW convection remains near the coastal region over both land and ocean, suggesting model deficiencies in depicting precipitation processes over the Guinea Highlands. Important influences of topography over the Guinea Highlands on AEWs and downstream TC genesis have also been suggested by several previous observational and modeling studies (e.g., Daloz et al. 2012; Ventrice et al. 2012b; Martin and Thorncroft 2015).

It is noteworthy that the AEW rainfall evolution patterns based on rainfall from the ERA5 reanalysis model output show very similar features to those based on GPM in Fig. 5a although with a slightly weaker amplitude (figure not shown),

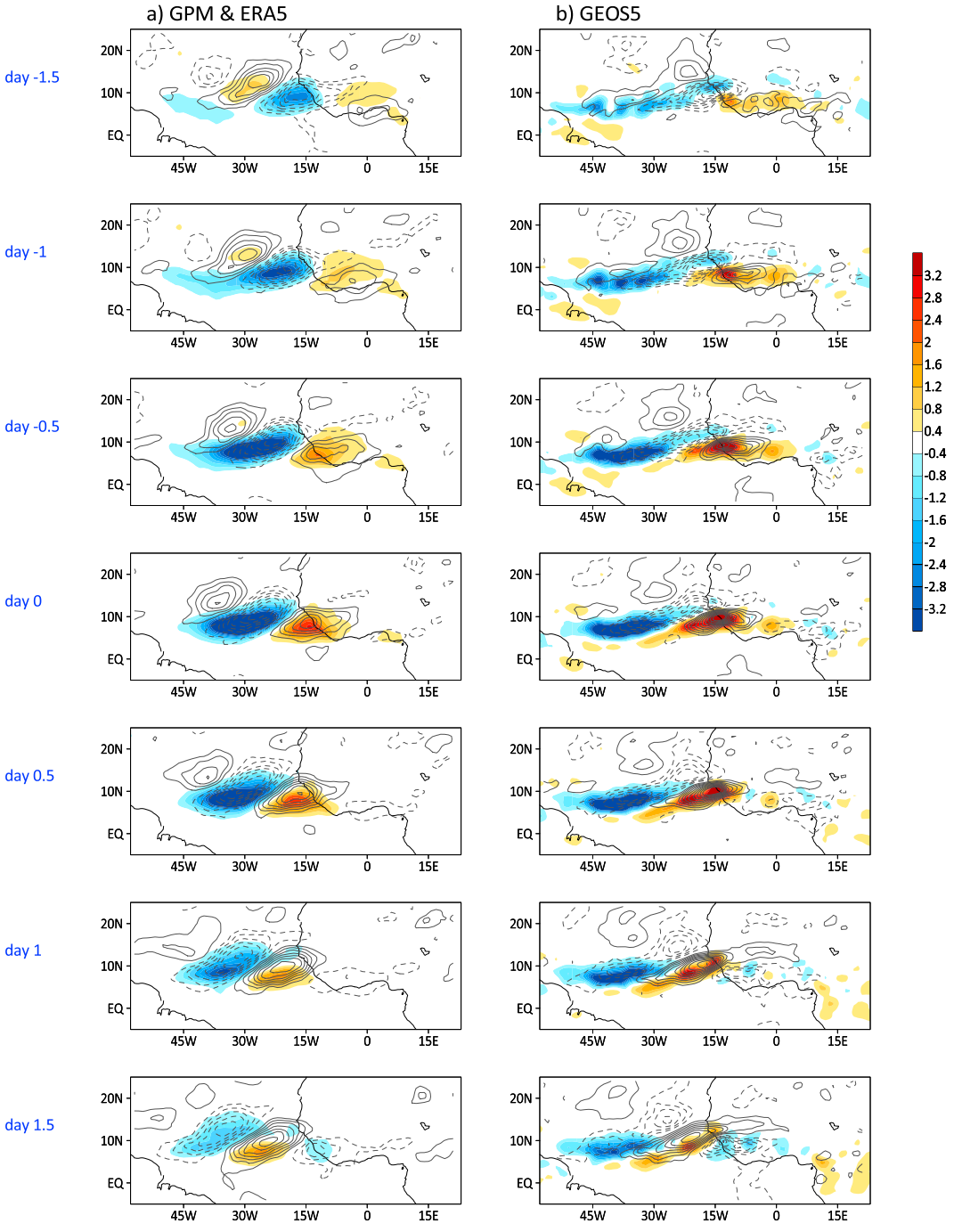

FIG. 5. Evolution of AEW precipitation (shaded with color bar; mm day^{-1}) and 650-hPa relative vorticity anomalies (contours with intervals of 0.5 × 10^{-6} s^{-1}; solid and dashed contours for positive and negative values) based on (a) observations and (b) GEOS-5 simulations. These precipitation and vorticity anomalies are derived by lag-regressions of 2–6-day bandpass filtered anomalies against the time series of the leading EOF modes that capture the AEW waves based on both observations and GEOS-5 simulations. See text for details.

similar to that previously reported for the Madden–Julian oscillation (Jiang et al. 2019). This lends additional confidence to use the ERA5 reanalysis to characterize the vertical structure of AEWs in the following section.

Zonal propagation of precipitation and 650-hPa relative vorticity anomalies associated with AEWs in observations and GEOS-5 are further illustrated in Fig. 6. A smooth westward propagation of both precipitation (shaded) and vorticity

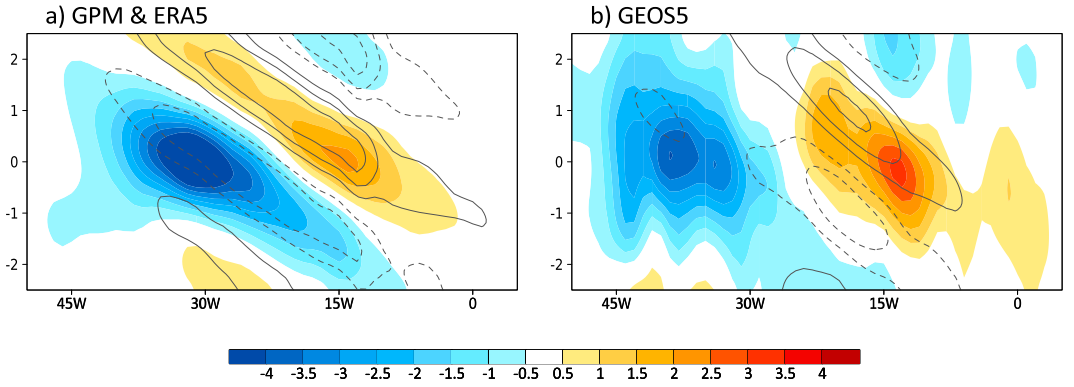

FIG. 6. Longitude–time evolution of AEW precipitation (shaded; mm day^{-1}) and 650-hPa relative vorticity anomalies (contours with intervals of 0.5×10^{-6} s^{-1}) based on evolution patterns in Fig. 5 for (a) observations and (b) GEOS-5 simulations.

(contours) are readily seen in the observations (Fig. 6a), at a phase speed of about 8° day^{-1}, consistent with many previous reports (e.g., Carlson 1969; Burpee 1972; Hsieh and Cook 2005). While enhanced (suppressed) precipitation is largely in phase with positive (negative) vorticity, Fig. 6a suggests that a trough (ridge) slightly leads the observed positive (negative) convection center. In GEOS-5, as previously discussed, both the westward propagation of convection and vorticity are largely limited to the east of 30°W, with a slower propagation speed of 6° day^{-1}. More or less standing precipitation anomalies over the coastal region near 15°W are clearly seen. To the west of 30°W, while vorticity anomalies of AEWs are almost absent, suppressed precipitation anomalies largely display a stationary pattern and tend to exhibit an east–west seesaw variability with the convection over the coastal region near 15°W (Fig. 6b).

To explore the relative role of dynamic and thermodynamic effects on AEW precipitation anomalies, Fig. 7 shows spatial patterns of low-level divergence at 900 hPa and lower-tropospheric buoyancy (B_L) anomalies associated with AEWs along with precipitation anomalies at day 0 in both observations and GEOS-5 simulations. Analysis of B_L anomalies associated with AEWs is mainly motivated by the close relationship between B_L and tropical precipitation in recent studies (Ahmed and Neelin 2018; Ahmed et al. 2020; Ahmed and Neelin 2021). One advantage in using B_L is that B_L anomalies

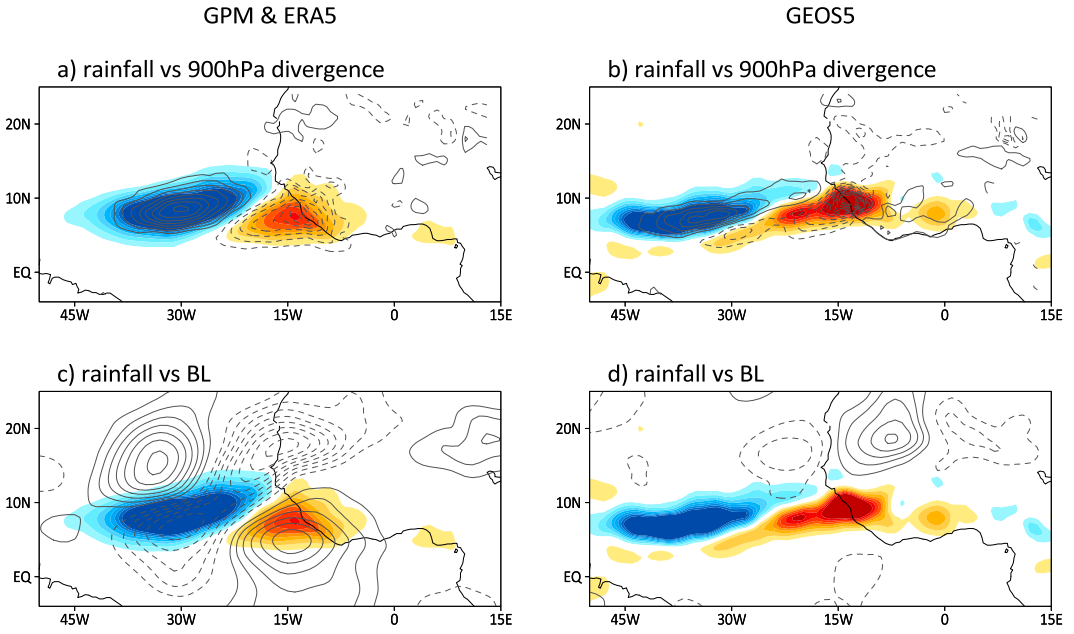

FIG. 7. Spatial patterns of (a),(b) precipitation anomalies (shaded; mm day^{-1}) associated with AEWs at day 0 along with 900-hPa divergence (contours, with intervals of 0.5×10^{-6} s^{-1}) and (c),(d) low-tropospheric buoyancy anomalies (contours with intervals of 1×10^{-3} m s^{-2}) for (left) observations and (right) GEOS-5 simulations.

can represent variability from both temperature and moisture anomalies. The B_L is calculated between the top of boundary layer (a 150-hPa depth from the surface) and 500 hPa following Ahmed and Neelin (2021), which can be further decomposed into lower-tropospheric measures of moisture subsaturation (q_L) and undiluted conditional instability [equivalent to the convective available potential energy (CAPE_L)].

Figure 7 clearly illustrates that precipitation anomalies associated with AEWs closely correspond to low-level convergence (Figs. 7a,b) rather than B_L (Figs. 7c,d) in both observations and simulations. In the observations, as positive (negative) B_L anomalies are present over positive (negative) rainfall regions, thermodynamic conditions can also play an important role for the development of AEW convection (e.g., Janiga and Thorncroft 2016), although the relative role of dynamic versus thermodynamic forcing needs to be further investigated. The lack of anomalous B_L signals to south of 10°N in GEOS-5 simulations could be associated with rather weak moisture variability in the model compared to the observations, as will be further discussed in the following. As a result, modulation of AEW convection in the model is largely controlled by the dynamic lifting. Decomposition of B_L anomalies in the observations into q_L and CAPE_L suggests that to the south of 10°N over the ITCZ region, B_L is largely dominated by the moisture effect q_L which is largely consistent with previous studies; while to the north of 10°N, both q_L and CAPE_L play similar roles (figure not shown).

d. *Vertical structures of AEWs*

In this subsection, vertical structures of AEWs in observations and GEOS-5 simulations are explored. Figure 8 illustrates vertical–longitude profiles of relatively vorticity, divergence, and meridional–vertical motion associated with AEWs. The observed AEW vorticity anomalies exhibit a barotropic structure from surface to 300 hPa without obvious vertical tilting (Fig. 8a), consistent with previous studies showing that vertical wind shear–induced baroclinic instability may play a minor role for AEWs over the Atlantic along the south track (e.g., Hsieh and Cook 2008; Russell and Aiyyer 2020). These strong vorticity anomalies in the lower troposphere can effectively modulate cyclogenesis (e.g., Emanuel and Nolan 2004; Jiang et al. 2012; Russell et al. 2017). In GEOS-5 simulations (Fig. 8b), while the vertical vorticity structure associated with enhance AEW precipitation near 15°W is largely similar to the observations, the negative vorticity corresponding to the suppressed convection near 30°W is less well organized and rather weak in the low levels. Consistent with weak vorticity anomalies near 30°W in GEOS-5 simulations, weak lower-level divergence/upper-level convergence and downward motions are also noted associated with local suppressed AEW convection, while these fields associated with enhanced AEW convection near 15°W are largely comparable to their observed counterparts (cf. Figs. 7d,f vs Figs. 7c,e). As indicated by the vertical velocity profiles, much weaker diabatic heating in model simulations compared to the observation, particularly in the lower-troposphere near 30°W, will greatly weaken local PV generation, which has been found to play a critical role in sustaining AEWs (e.g., Berry and Thorncroft 2005; Hsieh and Cook 2007; Janiga and Thorncroft 2013, 2014).

Vertical–longitudinal profiles of specific humidity and temperature anomalies of AEWs in both ERA5 and GEOS-5 simulations along with those in AIRS observations are further illustrated in Fig. 9. As only twice daily data are available from AIRS, the vertical profiles shown in Fig. 9 are derived based on regressions at day 0 onto the daily PC_1 time series obtained from the original 3-hourly PC time series of AEW indices for observations and simulations. Also, due to a large number of missing data on individual grids in daily AIRS observations, daily mean T and q are first averaged over the 5°–15°N latitude band before removing the climatological annual cycle and 2–6-day time filtering, to obtain a full daily coverage of these two fields over the vertical–longitude domain shown in Fig. 9. Tests based on ERA5 and GEOS-5 data suggest that the regression patterns at day 0 based on daily and 6-hourly PC_1 time series are very similar (figure not shown). Figures 9a and 9b generally shows a vertically stacked specific humidity structure associated with AEWs in the observations, with enhanced (reduced) lower-to-mid-tropospheric moisture associated with active (suppressed) AEW convection. The amplitude of moisture anomalies in GEOS-5 again is rather weak compared to AIRS and ERA5, particularly over the downstream region near 30°W, consistent with previous discussions on model biases in simulating the B_L pattern (Fig. 7d). Additionally, over the West African coast near 15°W, the maximum moisture is found near 600 hPa rather than a low-level maximum near or below 750 hPa in AIRS and ERA5. This can be further related to model biases in representing the AEW precipitation over the coastal region near the Guinea Highlands as shown in Fig. 5b.

Largely similar vertical T structures associated with AEWs are seen among AIRS, ERA5, and GEOS-5 simulations, with positive T anomalies in the midtroposphere and opposite signs below and above, although again with a much weaker amplitude in GEOS-5 simulations. Negative T anomalies in the lower troposphere below 600 hPa over the enhanced AEW rainfall region can be associated evaporative cooling of precipitation. Collocation of warm anomalies in the midtroposphere with upward motion (see Figs. 9d–f and 8e,f) is associated with enhanced AEW convection, suggesting a baroclinic energy conversion from eddy available potential energy to kinetic energy.

While largely similar vertical structures of moisture and temperature associated with AEWs are found between AIRS and ERA5, differences are also noted between them, particularly in the temperature structures (Figs. 9d,e). For example, generally weaker amplitude in temperature anomalies is seen in AIRS, particularly in the lower troposphere. Meanwhile, AIRS temperature anomalies in the upper troposphere appear at a higher altitude. This may be associated with possible deficiencies in ERA5, but could also be attributed to the different sampling between these two datasets, including the frequency of the data availability (twice daily for AIRS versus 6-hourly for ERA5 used for this study), and also missing observations particularly the low sampling over cloudy regions involved with AIRS data (Tian et al. 2013).

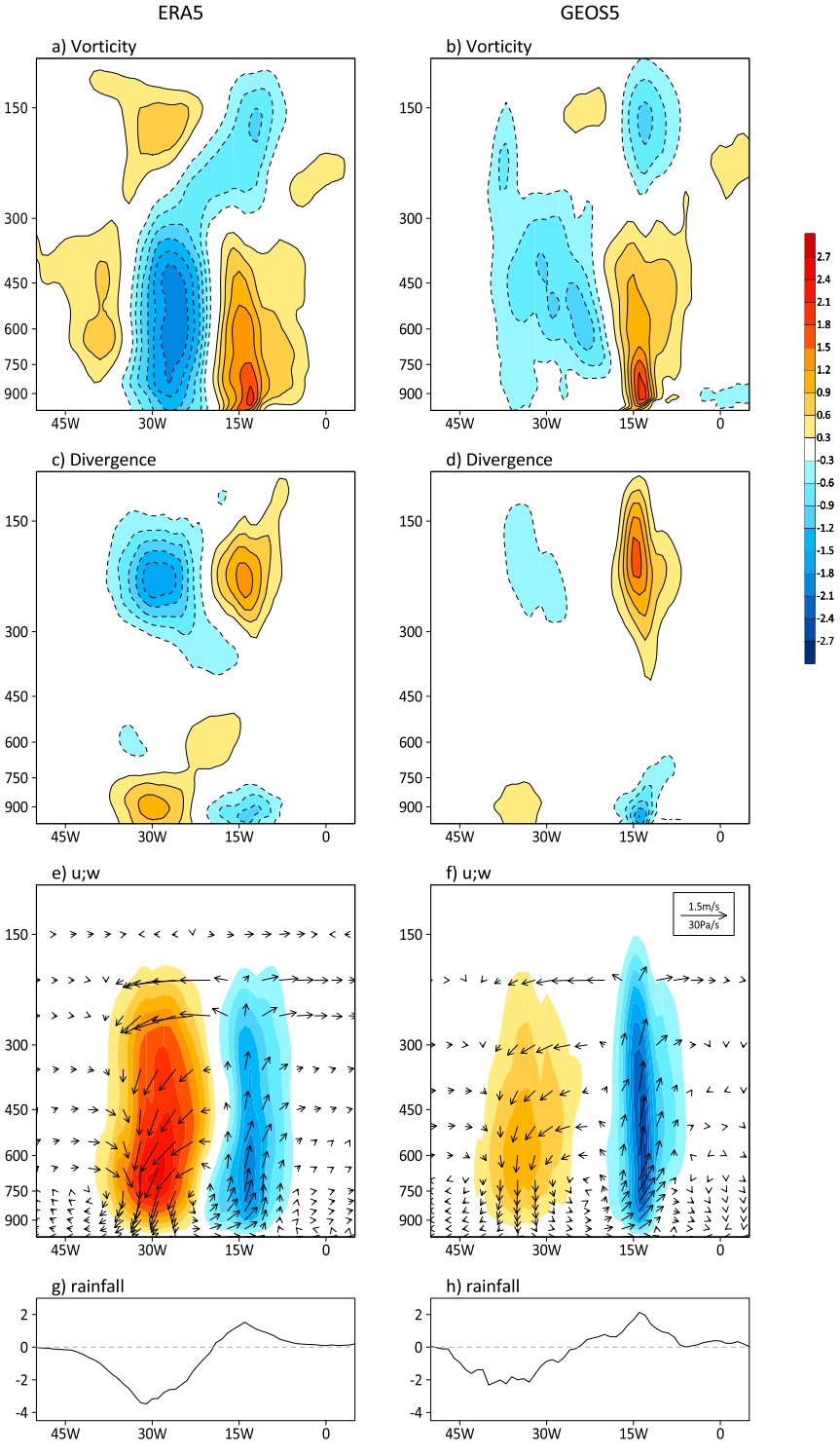

FIG. 8. Vertical–longitudinal cross sections (averaged over 5°–15°N) of (a),(b) relative vorticity (see color bar with units of 1×10^{-6} s^{-1}), (c),(d) divergence (color bar with units of 1×10^{-6} s^{-1}), and (e),(f) zonal–vertical wind vectors [see scale at upper-right of (f); direction of the vertical p velocity is reversed along with vertical p velocity in shading with intervals of 10^{-3} Pa s^{-1}] associated with AEWs at day 0 based on (left) ERA5 and (right) GEOS-5 simulations. (g),(h) Corresponding longitudinal profiles of precipitation anomalies over the same latitude bands are also shown for both observations and GEOS-5 simulations.

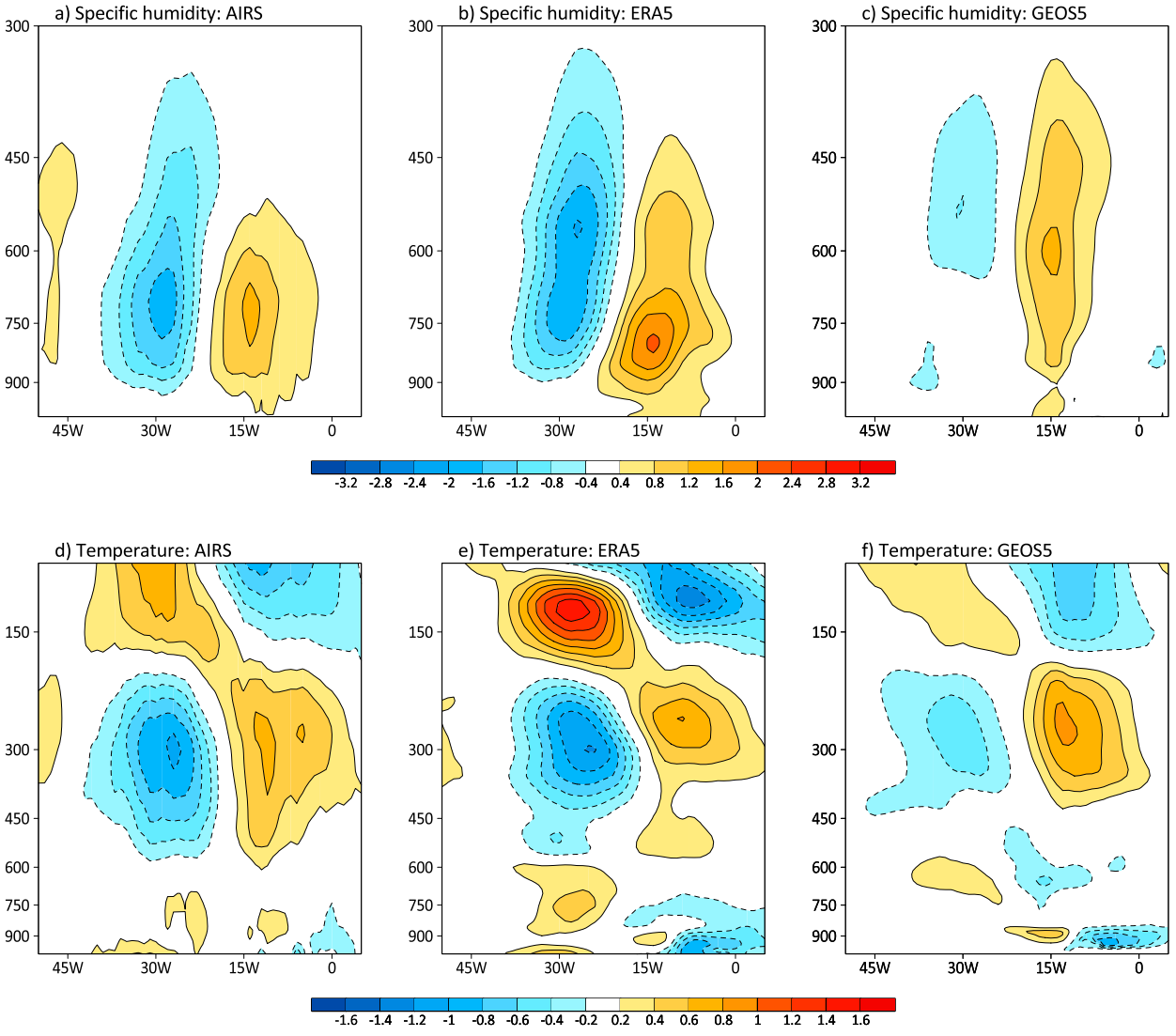

FIG. 9. As in Fig. 8, but for vertical–longitudinal cross sections of (a)–(c) specific humidity (10^{-1} g kg^{-1}) and (d)–(f) temperature (10^{-1} K) anomalies based on (left) AIR satellite observations, (center) ERA5 reanalysis, and (right) GEOS-5 simulations.

e. *Possible processes responsible for model deficiencies in simulating AEWs*

Based on the discussions above, the weak AEW signals downstream off the African coast in GEOS-5 could be due to slow westward propagation of AEWs (Fig. 6b), which may be related to model deficiencies in representing convection over the Guinea Highlands (Fig. 5b). Meanwhile, the very narrow and nearly east–west-oriented AEW circulation due to strong horizontal stretching to the south of 10°N in the model (Fig. 5b) may prevent downstream deep convection from being effectively organized because of a weak rotational component and thus weak low-level convergence through frictional effects. It has been previously suggested that, in addition to the dynamical instability of the local environment, strong convective coupling also plays a critical role in sustaining the growth of AEWs over the Atlantic through generation of eddy available potential energy by diabatic heating (e.g., Hsieh and Cook 2007) or the generation of PV due to vertical gradient of diabatic heating in the lower troposphere (e.g., Janiga and Thorncroft 2013; Russell and Aiyyer 2020).

Figure 10 examines energetics of AEWs in both ERA5 and GEOS-5 by illustrating time-integrated covariance patterns of $\overline{u'v'}$, $\overline{v'T'}$, and $\overline{w'T'}$, which represent conversions from zonal kinetic energy (K_Z) to eddy kinetic energy (K_E), from zonal available potential energy (A_Z) to eddy available potential energy (A_E), and from A_E to K_E, respectively. The variables with prime represent 6-hourly anomalous fields associated with AEWs obtained by lag regressions against AEW indices based on the leading PCs. The overbar above these covariance terms represents integrations for the period from day −4 to day 4 following Kiladis et al. (2006), roughly corresponding to two full cycles of AEW variability.

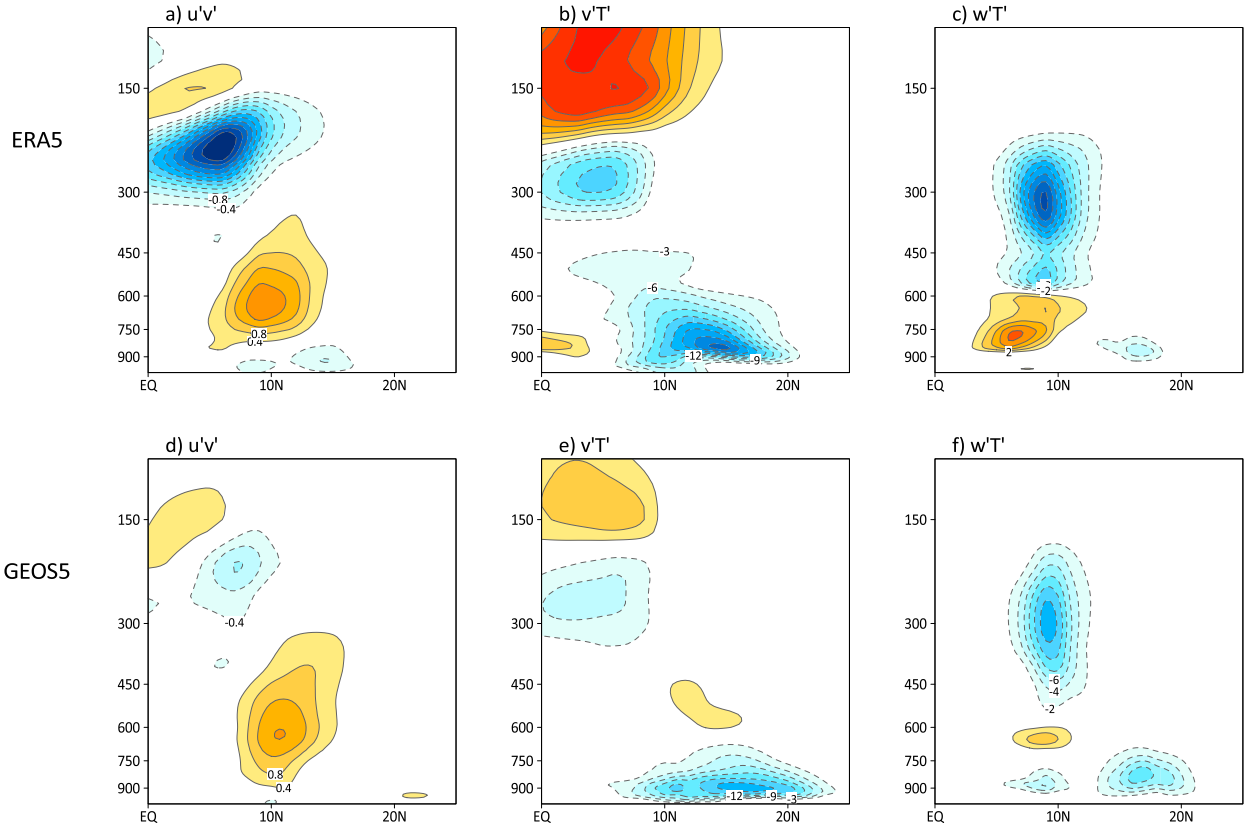

FIG. 10. Meridional–vertical cross sections (averaged over 30°W–10°E) of time-integrated covariance terms from day −4 to day 4 of (left) $\overline{u'v'}$, (center) $\overline{v'T'}$, and (right) $\overline{w'T'}$ based on (a)–(c) ERA5 and (d)–(f) GEOS-5 simulations. All these anomalous fields associated with AEWs are derived based on lag-regressions onto the corresponding leading PCs of precipitation EOF_1 based on observations and GEOS-5 simulations.

Results on the energetics of AEWs based on ERA5 shown in Fig. 10 are largely similar to previous studies (e.g., Norquist et al. 1977; Diedhiou et al. 2002; Hall et al. 2006; Kiladis et al. 2006). The maximum positive $\overline{u'v'}$ is found to the south flank of AEJ near 650 hPa (15°N, Fig. 1), suggesting barotropic energy conversions from K_Z to K_E. This is also consistent with the observed southwest–northeast tilt in AEW vorticity fields (Fig. 5a). Meanwhile, AEW K_E is also contributed from the baroclinic conversion from A_E to K_E, namely through covariance between warm anomalies and upward motion in the midtroposphere ($\overline{w'T'}$; Fig. 10c). In turn, the A_E term can be supplied from A_Z through strong negative meridional temperature fluxes ($\overline{v'T'}$) with a maximum located below 600 hPa to the south of 20°N (Fig. 10b). Considering the northward gradient of mean temperature in the low levels to the south of 20°N, this downgradient temperature transport in the low level is consistent with the baroclinic instability.

Strong barotropic conversion associated with positive $\overline{u'v'}$ to the south of the AEJ is also evident in GEOS-5 simulations, with a largely comparable amplitude to that based on ERA5 (Fig. 10d). This is also consistent with the very strong southwest–northeast horizontal stretching in AEW vorticity in GEOS-5 simulations (Fig. 5b). However, the baroclinic energy conversion term ($\overline{w'T'}$; Fig. 10f) and meridional heating fluxes ($\overline{v'T'}$; Fig. 10e) are both weaker in GEOS-5 simulations.

A recent PV budget analysis by Russell and Aiyyer (2020) suggested that the westward propagation of AEWs over the Atlantic is mainly due to two processes, one through advection of AEW PV by the background flow and another through advection of the background PV by AEW circulation. For the first process, the easterly mean flow of the AEJ plays a crucial role for AEW westward propagation as a steering flow. The second process involves interactions of counterpropagating Rossby waves over a region with reversed meridional PV gradient over the Atlantic. For example, a westward (eastward) propagating wave prevails over the region of a positive (negative) meridional PV gradient. Interactions between the eastward and westward propagating waves will lead to the barotropic instability for AEWs and associated horizontal tilting wave structures as observed in Fig. 5a (Russell and Aiyyer 2020; Hoskins et al. 1985). Therefore, to further understand possible processes responsible for the slow westward propagation of AEWs and strong horizontal stretching in AEW circulation pattern in GEOS-5 simulations as discussed in Fig. 5b, we further compared summer mean zonal wind and meridional PV gradient between ERA5 and GEOS-5 simulations.

Figures 11a and 11b show vertical–latitudinal profiles of summer mean meridional PV gradient (shaded) along with mean zonal wind (contours) averaged over the 30°W–10°E

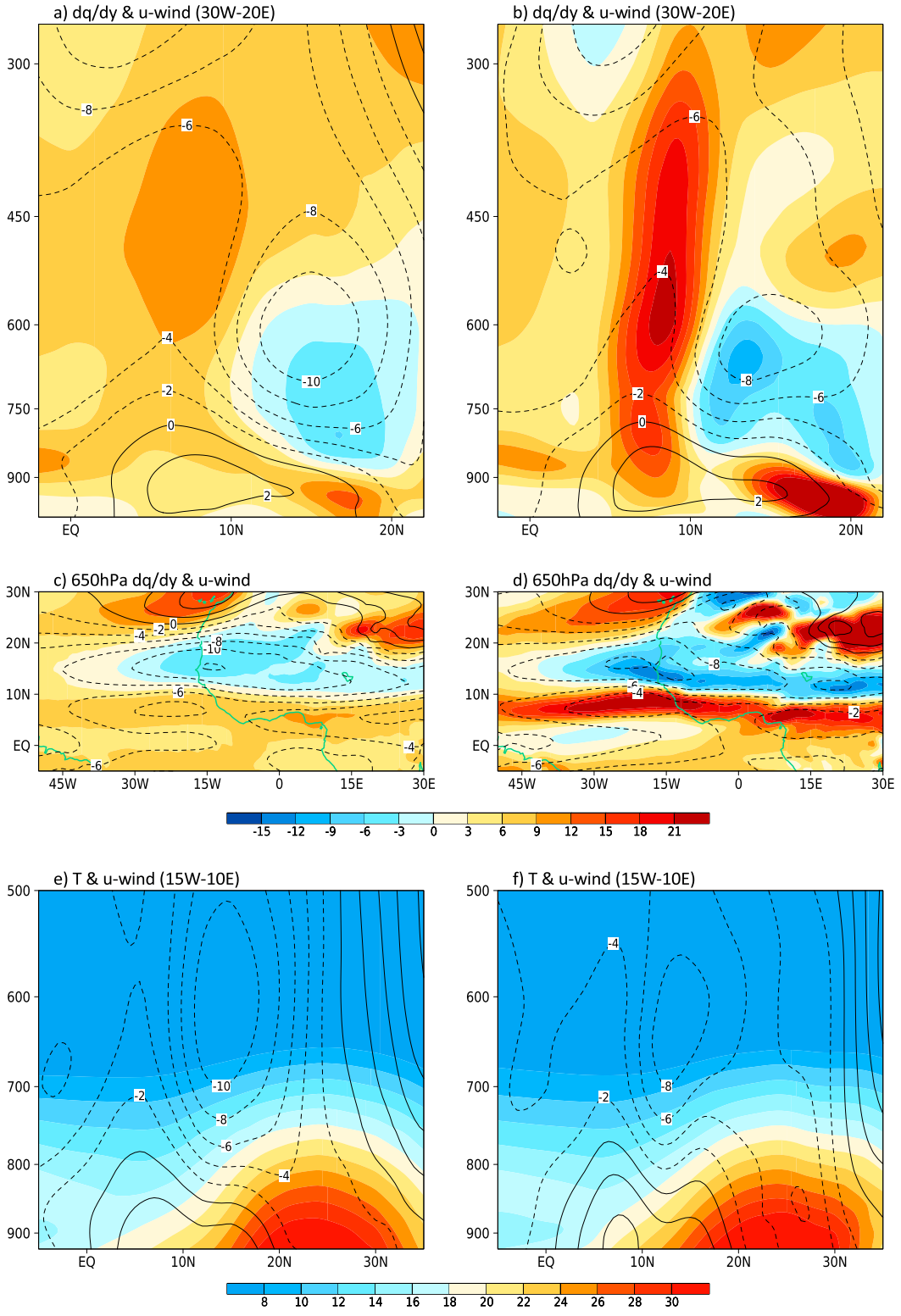

FIG. 11. (a),(b) Vertical–latitudinal cross sections (averaged over 30°W–10°E) of the meridional gradient of summer mean potential vorticity [shaded with color bar below (c) and (d); 10^{-7} km^2 kg^{-1} s^{-1}] and zonal wind (contours; m s^{-1}). (c),(d) Spatial distribution of summer mean potential vorticity (shaded; 10^{-7} km^2 kg^{-1} s^{-1}) and zonal wind (contours with intervals of 2 m s^{-1}) at 650 hPa. (e),(f) As in (a) and (b), but for vertical–latitudinal cross sections of summer mean temperature (shaded; °C) and zonal wind (contours; m s^{-1}) for (left) observations and (right) GEOS-5 simulations.

longitude band. Similar to Fig. 2, a weaker AEJ is noted in GEOS-5 simulations (8 m s^{-1}) compared the observations (10 m s^{-1}). As previously discussed, this can possibly lead to a slower westward propagation speed of AEWs in GEOS-5 (Fig. 6). Further analysis suggests that the weaker AEJ in GEOS-5 can be associated with the relatively weaker meridional gradient in summer mean temperature as indicated by a slightly flatter vertical slope in the mean temperature pattern near 15°N below 850 hPa in GEOS-5. The averaged meridional T gradient over 10°–20°N and 925–800 hPa is 1.76 and 1.71 K per degree in ERA5 and GEOS-5, respectively. Since the observed SST is specified in GEOS-5 simulations, this relatively weaker meridional temperature gradient in GEOS-5 could be ascribed to model deficiencies in representing low-level temperature over the Sahel region. While a reversal in the observed meridional PV gradient near 10°N in the lower troposphere between 900 and 500 hPa (Fig. 11a) is captured in GEOS-5 (Fig. 11b), which thus meets a necessary condition for instability to sustain the growth of AEWs (Charney and Stern 1962), GEOS-5 overestimates both the positive PV gradient to the south of 10°N and the negative PV gradient to the north of 10°N, when compared with observations. As the southwest–northeast horizontal tilting of the AEW vorticity pattern to the south of the AEJ core (as in Fig. 5) is largely due to the positive mean PV meridional gradient over this region, the much stronger PV gradient in GEOS-5 simulations thus could be responsible for the strong east–west stretching in model AEW patterns. Further sensitivity tests by calculating PV based on switched summer mean T, u, and v winds between ERA5 and GEOS-5 simulations suggest that the significant difference in PV gradient to the south 10°N is mainly due to the differences in u wind. As shown in Fig. 11b, the strong positive PV gradient to the south of 10°N in GEOS-5 is largely collocated with a local u-wind maximum stretching the troposphere. The stronger positive (negative) PV gradient to the south (north) of 10°N in GEOS-5 simulations and its close association of mean zonal wind can be further clearly seen in the spatial patterns at 650 hPa (Figs. 11c,d). Note that since the location corresponding to the maximum positive PV gradient in GEOS-5 is largely collocated with the ITCZ, model biases in representing convective processes over the Atlantic ITCZ region may also play a role with regard to the biases in the PV gradient as previously proposed (e.g., Schubert et al. 1991; Hsieh and Cook 2008). On the other hand, we cannot exclude the possibility that generally weaker AEW activity in GEOS-5 could also lead to stronger PV gradient as less energy is extracted from the mean circulation. These results thus suggest high sensitivity of simulated AEW characteristics to large-scale environment, which has also been found in previous idealized model simulations (e.g., Hall et al. 2006).

4. Summary and discussion

Considering the significant influence of AEWs on local and downstream high-impact weather extremes, a better understanding of key processes in regulating AEWs and skillful representation of AEWs in climate and weather prediction models are important. In this study, the simulation of AEWs in the NASA GEOS-5 AGCM, including their evolution, vertical structures, and linkage to Atlantic TC genesis, is examined and compared to ERA5 reanalysis and satellite observations.

Different from previous studies that identified AEWs based on circulation and convection proxies including the outgoing longwave radiation (OLR) and T_B, precipitation data are used to identify AEWs for both observations and GEOS-5 simulations in this study by applying an EOF analysis over the Atlantic and West African sectors. While the leading EOF modes in GEOS-5 capture the observed westward propagating AEWs along the southern track near 10°N off the Guinea coast, several significant deficiencies are noted in simulated AEWs. The AEW wave patterns in GEOS-5 exhibit a strong horizontal stretching over the Atlantic, forming a very narrow and nearly east–west oriented vorticity band. The model AEWs also experience a slower westward propagation that is largely confined to the east of 30°W. This slow westward propagation in GEOS-5 tends to be associated with too persistent precipitation near the Guinea Highlands region, in contrast to the occurrence of maximum AEW precipitation over the ocean in the observations. It is also illustrated that AEWs in GEOS-5 simulations become significantly weakened downstream to the west of 20°W. The well-organized AEW structures in the observations, with vertically stretched vorticity and vertical motion from near the surface to the upper troposphere, are not well simulated in GEOS-5, particularly with rather weak signals in the lower troposphere. The weak AEW circulation downstream along the south track could be responsible for the rather suppressed TC genesis over the MDR in GEOS-5 simulations although there exist controversial opinions on the role of synoptic disturbances in determining the climatology of TC genesis over the Atlantic.

Further analyses suggest that model deficiencies in summer mean zonal wind and associated meridional potential vorticity gradient over the Atlantic sector could be related to the above-mentioned model biases in AEW simulations. Since the AEJ plays a primary role in steering the westward propagation of AEWs based on observational studies, a slightly weaker AEW strength in GEOS-5 simulations could partially lead to the less systematic westward propagation of AEWs in the model. Moreover, although a reversal of meridional PV gradient in the lower troposphere, a necessary condition for instability to sustain growth of AEWs, is simulated in GEOS-5, both the amplitudes of negative meridional PV gradient to the north of 10°N and particularly positive gradient to south of 10°N are greatly overestimated. Associated with the counter-propagating Rossby waves in the two regions with opposite meridional PV gradients, the overestimated PV gradient to the north of 10°N is expected to slow the AEW westward propagation speed, while biases in the positive PV gradient to the south of 10°N can lead to extremely strong southwest–northeastward tilting in AEW structure as seen in GEOS-5 simulations. The very narrow and horizontally stretched AEW circulation in model simulations can prevent the deep convection from being effectively organized due to a rather weak rotational component in the circulation. A lack of strong AEW–convection

coupling can thus further lead to weak AEWs downstream. As the meridional PV gradient corresponds to the Laplacian of zonal wind, therefore minor deficiencies in mean zonal wind meridional profile can lead to significant biases in PV gradient, and thus significantly affect characteristics of AEWs in model simulations. A strong sensitivity of AEW response to the mean circulation has been suggested in idealized model simulations (e.g., Hall et al. 2006). It thus represents a great challenge for climate models to accurately simulate AEW activity and its variability. A future study could further explore the detailed influences of the amplitude of PV gradients on organization of AEWs and associated energetics based on idealized model simulations.

Future investigations are also warranted to understand processes involved with interactions between AEW and convection over the West Africa coast in the region of the Guinea Highlands. As previously discussed, GEOS-5 shows too persistent and vigorous convection associated with AEWs over this region, in contrast to the maximum AEW convection over the ocean. It is expected that improved simulations that capture interactions between AEW circulation and convection over the Guinea Highlands will lead to improvement of propagation speed of simulated AEWs in GEOS-5. Importance of convective systems over the Guinea Highlands for strengthening downstream AEW development has also been suggested in previously studies (Ventrice et al. 2012b; Janiga and Thorncroft 2014; Martin and Thorncroft 2015). Further studies will also be conducted to explore physical processes related to the initiation of AEW convection near the Gulf of Guinea as suggested by GPM precipitation observations. It is also noteworthy that by using a rainfall-based AEW index, this study mainly focuses on convective activity of the AEWs over the West Africa coast and Atlantic Ocean. Dry AEWs that can be identified by a circulation index as in many previous studies are not included in this study.

While ERA5 reanalysis and AIRS observations are used in this study to characterize detailed 3D structures of AEWs, in situ observations of convection, clouds, and circulations associated with AEWs, for example, from the Convective Processes Experiment–Aerosols and Winds (CPEX-AW) campaign, will provide critical validations and insights into detailed processes governing the propagation and maintenance of AEWs.

Acknowledgments. XJ, HS, and SSC acknowledge the funding support by the NASA CPEX-AW Grant 80NSSC20K0895 and the NASA WAAD program. PAU acknowledges support of the U.S. Department of Energy, Office of Science, Office of Biological and Environmental Research program under Award Number DE-SC0016605. We thank Dr. Matt Janiga and two anonymous reviewers for their insightful comments on an earlier version of this manuscript.

Data availability statement. The GPM rainfall data used for this study can be accessed from the website https://disc.gsfc.nasa.gov/datasets/GPM_3IMERGHH_06/summary?keywords=GPM%20IMERG. AIRS data were downloaded from https://disc.gsfc.nasa.gov/datasets/AIRS3STD_006/summary?keywords=AIRS. The ERA5 data were downloaded from the website https://cds.climate.copernicus.eu/cdsapp#!/dataset/reanalysis-era5-pressure-levels. GEOS-5 AMIP simulations were obtained downloaded from https://portal.nccs.nasa.gov/datashare/gmao_m2amip/.

REFERENCES

Aarons, Z. S., S. J. Camargo, J. D. O. Strong, and H. Murakami, 2021: Tropical cyclone characteristics in the MERRA-2 reanalysis and AMIP simulations. *Earth Space Sci.*, **8**, e2020EA001415, https://doi.org/10.1029/2020EA001415.

Ahmed, F., and J. D. Neelin, 2018: Reverse engineering the tropical precipitation–buoyancy relationship. *J. Atmos. Sci.*, **75**, 1587–1608, https://doi.org/10.1175/JAS-D-17-0333.1.

——, and ——, 2021: A process-oriented diagnostic to assess precipitation–thermodynamic relations and application to CMIP6 models. *Geophys. Res. Lett.*, **48**, e2021GL094108, https://doi.org/10.1029/2021GL094108.

——, Á. F. Adames, and J. D. Neelin, 2020: Deep convective adjustment of temperature and moisture. *J. Atmos. Sci.*, **77**, 2163–2186, https://doi.org/10.1175/JAS-D-19-0227.1.

Alaka, G. J., Jr., and E. D. Maloney, 2012: The influence of the MJO on upstream precursors to African easterly waves. *J. Climate*, **25**, 3219–3236, https://doi.org/10.1175/JCLI-D-11-00232.1.

Albignat, J. P., and R. J. Reed, 1980: The origin of African wave disturbances during phase III of GATE. *Mon. Wea. Rev.*, **108**, 1827–1839, https://doi.org/10.1175/1520-0493(1980)108<1827:TOOAWD>2.0.CO;2.

Avila, L. A., R. J. Pasch, and J.-G. Jiing, 2000: Atlantic tropical systems of 1996 and 1997: Years of contrasts. *Mon. Wea. Rev.*, **128**, 3695–3706, https://doi.org/10.1175/1520-0493(2000)128<3695:ATSOAY>2.0.CO;2.

Bacmeister, J. T., and G. L. Stephens, 2011: Spatial statistics of likely convective clouds in CloudSat data. *J. Geophys. Res.*, **116**, D04104, https://doi.org/10.1029/2010JD014444.

——, M. J. Suarez, and F. R. Robertson, 2006: Rain reevaporation, boundary layer–convection interactions, and Pacific rainfall patterns in an AGCM. *J. Atmos. Sci.*, **63**, 3383–3403, https://doi.org/10.1175/JAS3791.1.

Bercos-Hickey, E., and C. M. Patricola, 2021: Anthropogenic influences on the African easterly jet–African easterly wave system. *Climate Dyn.*, **57**, 2779–2792, https://doi.org/10.1007/s00382-021-05838-1.

Berry, G. J., and C. Thorncroft, 2005: Case study of an intense African easterly wave. *Mon. Wea. Rev.*, **133**, 752–766, https://doi.org/10.1175/MWR2884.1.

Brannan, A. L., and E. R. Martin, 2019: Future characteristics of African easterly wave tracks. *Climate Dyn.*, **52**, 5567–5584, https://doi.org/10.1007/s00382-018-4465-z.

Burpee, R. W., 1972: The origin and structure of easterly waves in the lower troposphere of North Africa. *J. Atmos. Sci.*, **29**, 77–90, https://doi.org/10.1175/1520-0469(1972)029<0077:TOASOE>2.0.CO;2.

——, 1974: Characteristics of North African easterly waves during the summers of 1968 and 1969. *J. Atmos. Sci.*, **31**, 1556–1570, https://doi.org/10.1175/1520-0469(1974)031<1556:CONAEW>2.0.CO;2.

Carlson, T. N., 1969: Synoptic histories of three African disturbances that developed into Atlantic hurricanes. *Mon. Wea. Rev.*,

97, 256–276, https://doi.org/10.1175/1520-0493(1969)097<0256:SHOTAD>2.3.CO;2.

Chahine, M. T., and Coauthors, 2006: AIRS: Improving weather forecasting and providing new data on greenhouse gases. *Bull. Amer. Meteor. Soc.*, **87**, 911–926, https://doi.org/10.1175/BAMS-87-7-911.

Charney, J. G., and M. E. Stern, 1962: On the stability of internal baroclinic jets in a rotating atmosphere. *J. Atmos. Sci.*, **19**, 159–172, https://doi.org/10.1175/1520-0469(1962)019<0159:OTSOIB>2.0.CO;2.

Chen, T.-C., S.-Y. Wang, and A. J. Clark, 2008: North Atlantic hurricanes contributed by African easterly waves north and south of the African easterly jet. *J. Climate*, **21**, 6767–6776, https://doi.org/10.1175/2008JCLI2523.1.

Cheng, Y.-M., C. D. Thorncroft, and G. N. Kiladis, 2019: Two contrasting African easterly wave behaviors. *J. Atmos. Sci.*, **76**, 1753–1768, https://doi.org/10.1175/JAS-D-18-0300.1.

Collow, A. B. M., S. P. Mahanama, M. G. Bosilovich, R. D. Koster, and S. D. Schubert, 2017: An evaluation of teleconnections of the United States in an ensemble of AMIP simulations with the MERRA-2 configuration of the GEOS atmospheric model. NASA Tech. Rep. NASA/TM-2017-104606/Vol. 47, 78 pp., https://gmao.gsfc.nasa.gov/pubs/docs/Collow963.pdf.

Crétat, J., E. K. Vizy, and K. H. Cook, 2015: The relationship between African easterly waves and daily rainfall over West Africa: Observations and regional climate simulations. *Climate Dyn.*, **44**, 385–404, https://doi.org/10.1007/s00382-014-2120-x.

Daloz, A. S., F. Chauvin, K. Walsh, S. Lavender, D. Abbs, and F. Roux, 2012: The ability of general circulation models to simulate tropical cyclones and their precursors over the North Atlantic main development region. *Climate Dyn.*, **39**, 1559–1576, https://doi.org/10.1007/s00382-012-1290-7.

Dickinson, M., and J. Molinari, 2000: Climatology of sign reversals of the meridional potential vorticity gradient over Africa and Australia. *Mon. Wea. Rev.*, **128**, 3890–3900, https://doi.org/10.1175/1520-0493(2001)129<3890:COSROT>2.0.CO;2.

Diedhiou, A., S. Janicot, A. Viltard, P. de Felice, and H. Laurent, 1999: Easterly wave regimes and associated convection over West Africa and tropical Atlantic: Results from the NCEP/NCAR and ECMWF reanalyses. *Climate Dyn.*, **15**, 795–822, https://doi.org/10.1007/s003820050316.

——, ——, ——, and P. de Félice, 2002: Energetics of easterly wave disturbances over West Africa and the tropical Atlantic: A climatology from the 1979–95 NCEP/NCAR reanalyses. *Climate Dyn.*, **18**, 487–500, https://doi.org/10.1007/s00382-001-0195-7.

Dieng, A. L., S. M. Sall, L. Eymard, M. Leduc-Leballeur, and A. Lazar, 2017: Trains of African easterly waves and their relationship to tropical cyclone genesis in the eastern Atlantic. *Mon. Wea. Rev.*, **145**, 599–616, https://doi.org/10.1175/MWR-D-15-0277.1.

Duchon, C. E., 1979: Lanczos filtering in one and two dimensions. *J. Appl. Meteor. Climatol.*, **18**, 1016–1022, https://doi.org/10.1175/1520-0450(1979)018<1016:LFIOAT>2.0.CO;2.

Duvel, J. P., 1990: Convection over tropical Africa and the Atlantic Ocean during northern summer. Part II: Modulation by easterly waves. *Mon. Wea. Rev.*, **118**, 1855–1868, https://doi.org/10.1175/1520-0493(1990)118<1855:COTAAT>2.0.CO;2.

Elless, T. J., and R. D. Torn, 2018: African easterly wave forecast verification and its relation to convective errors within the ECMWF ensemble prediction system. *Wea. Forecasting*, **33**, 461–477, https://doi.org/10.1175/WAF-D-17-0130.1.

Emanuel, K., 2022: Tropical cyclone seeds, transition probabilities, and genesis. *J. Climate*, **35**, 3557–3566, https://doi.org/10.1175/JCLI-D-21-0922.1.

——, and D. S. Nolan, 2004: Tropical cyclone activity and global climate. Preprints, *26th Conf. on Hurricanes and Tropical Meteorology*, Miami, FL, Amer. Meteor. Soc., 240–241, https://ams.confex.com/ams/26HURR/techprogram/paper_75463.htm.

Fink, A. H., and A. Reiner, 2003: Spatiotemporal variability of the relation between African easterly waves and West African squall lines in 1998 and 1999. *J. Geophys. Res.*, **108**, 4332, https://doi.org/10.1029/2002JD002816.

Frank, N. L., 1970: Atlantic tropical systems of 1969. *Mon. Wea. Rev.*, **98**, 307–314, https://doi.org/10.1175/1520-0493(1970)098<0307:ATSO>2.3.CO;2.

Grist, J. P., 2002: Easterly waves over Africa. Part I: The seasonal cycle and contrasts between wet and dry years. *Mon. Wea. Rev.*, **130**, 197–211, https://doi.org/10.1175/1520-0493(2002)130<0197:EWOAPI>2.0.CO;2.

Grogan, D. F. P., T. R. Nathan, and S.-H. Chen, 2016: Effects of Saharan dust on the linear dynamics of African easterly waves. *J. Atmos. Sci.*, **73**, 891–911, https://doi.org/10.1175/JAS-D-15-0143.1.

Gu, G., R. F. Adler, G. J. Huffman, and S. Curtis, 2004: African easterly waves and their association with precipitation. *J. Geophys. Res.*, **109**, D04101, https://doi.org/10.1029/2003JD003967.

Hall, N. M. J., G. N. Kiladis, and C. D. Thorncroft, 2006: Three-dimensional structure and dynamics of African easterly waves. Part II: Dynamical modes. *J. Atmos. Sci.*, **63**, 2231–2245, https://doi.org/10.1175/JAS3742.1.

Hersbach, H., and Coauthors, 2020: The ERA5 global reanalysis. *Quart. J. Roy. Meteor. Soc.*, **146**, 1999–2049, https://doi.org/10.1002/qj.3803.

Hopsch, S. B., C. D. Thorncroft, K. Hodges, and A. Aiyyer, 2007: West African storm tracks and their relationship to Atlantic tropical cyclones. *J. Climate*, **20**, 2468–2483, https://doi.org/10.1175/JCLI4139.1.

Hoskins, B. J., M. E. McIntyre, and A. W. Robertson, 1985: On the use and significance of isentropic potential vorticity maps. *Quart. J. Roy. Meteor. Soc.*, **111**, 877–946, https://doi.org/10.1002/qj.49711147002.

Hsieh, J.-S., and K. H. Cook, 2005: Generation of African easterly wave disturbances: Relationship to the African easterly jet. *Mon. Wea. Rev.*, **133**, 1311–1327, https://doi.org/10.1175/MWR2916.1.

——, and ——, 2007: A study of the energetics of African easterly waves using a regional climate model. *J. Atmos. Sci.*, **64**, 421–440, https://doi.org/10.1175/JAS3851.1.

——, and ——, 2008: On the instability of the African easterly jet and the generation of African waves: Reversals of the potential vorticity gradient. *J. Atmos. Sci.*, **65**, 2130–2151, https://doi.org/10.1175/2007JAS2552.1.

Huffman, G., D. T. Bolvin, E. J. Nelkin, and J. Tan, 2019: Integrated multi-satellite retrievals for GPM (IMERG) technical documentation. NASA Tech. Doc., 77 pp., https://gpm.nasa.gov/sites/default/files/document_files/IMERG_doc_190909.pdf.

Janiga, M. A., and C. D. Thorncroft, 2013: Regional differences in the kinematic and thermodynamic structure of African easterly waves. *Quart. J. Roy. Meteor. Soc.*, **139**, 1598–1614, https://doi.org/10.1002/qj.2047.

——, and ——, 2014: Convection over tropical Africa and the east Atlantic during the West African monsoon: Regional and diurnal variability. *J. Climate*, **27**, 4159–4188, https://doi.org/10.1175/JCLI-D-13-00449.1.

——, and ——, 2016: The influence of African easterly waves on convection over tropical Africa and the east Atlantic. *Mon. Wea. Rev.*, **144**, 171–192, https://doi.org/10.1175/MWR-D-14-00419.1.

Jiang, X., M. Zhao, and D. E. Waliser, 2012: Modulation of tropical cyclones over the eastern Pacific by the intraseasonal variability simulated in an AGCM. *J. Climate*, **25**, 6524–6538, https://doi.org/10.1175/JCLI-D-11-00531.1.

——, B. Xiang, M. Zhao, T. Li, S.-J. Lin, Z. Wang, and J.-H. Chen, 2018: Intraseasonal tropical cyclogenesis prediction in a global coupled model system. *J. Climate*, **31**, 6209–6227, https://doi.org/10.1175/JCLI-D-17-0454.1.

——, H. Su, and D. E. Waliser, 2019: A damping effect of the Maritime Continent for the Madden–Julian oscillation. *J. Geophys. Res. Atmos.*, **124**, 13 693–13 713, https://doi.org/10.1029/2019JD031503.

Kiladis, G. N., C. D. Thorncroft, and N. M. J. Hall, 2006: Three-dimensional structure and dynamics of African easterly waves. Part I: Observations. *J. Atmos. Sci.*, **63**, 2212–2230, https://doi.org/10.1175/JAS3741.1.

Knapp, K. R., M. C. Kruk, D. H. Levinson, H. J. Diamond, and C. J. Neumann, 2010: The International Best Track Archive for Climate Stewardship (IBTrACS): Unifying tropical cyclone data. *Bull. Amer. Meteor. Soc.*, **91**, 363–376, https://doi.org/10.1175/2009BAMS2755.1.

Lafore, J.-P., and Coauthors, 2017: A multi-scale analysis of the extreme rain event of Ouagadougou in 2009. *Quart. J. Roy. Meteor. Soc.*, **143**, 3094–3109, https://doi.org/10.1002/qj.3165.

Laing, A. G., R. Carbone, V. Levizzani, and J. Tuttle, 2008: The propagation and diurnal cycles of deep convection in northern tropical Africa. *Quart. J. Roy. Meteor. Soc.*, **134**, 93–109, https://doi.org/10.1002/qj.194.

Landsea, C. W., 1993: A climatology of intense (or major) Atlantic hurricanes. *Mon. Wea. Rev.*, **121**, 1703–1713, https://doi.org/10.1175/1520-0493(1993)121<1703:ACOIMA>2.0.CO;2.

——, and W. M. Gray, 1992: The strong association between western Sahelian monsoon rainfall and intense Atlantic hurricanes. *J. Climate*, **5**, 435–453, https://doi.org/10.1175/1520-0442(1992)005<0435:TSABWS>2.0.CO;2.

Lau, K.-H., and N.-C. Lau, 1990: Observed structure and propagation characteristics of tropical summertime synoptic scale disturbances. *Mon. Wea. Rev.*, **118**, 1888–1913, https://doi.org/10.1175/1520-0493(1990)118<1888:OSAPCO>2.0.CO;2.

Lavender, S. L., and A. J. Matthews, 2009: Response of the West African monsoon to the Madden–Julian oscillation. *J. Climate*, **22**, 4097–4116, https://doi.org/10.1175/2009JCLI2773.1.

Lock, A. P., A. R. Brown, M. R. Bush, G. M. Martin, and R. N. B. Smith, 2000: A new boundary layer mixing scheme. Part I: Scheme description and single-column model tests. *Mon. Wea. Rev.*, **128**, 3187–3199, https://doi.org/10.1175/1520-0493(2000)128<3187:ANBLMS>2.0.CO;2.

Machado, L. A. T., J. P. Duvel, and M. Desbois, 1993: Diurnal variations and modulation by easterly waves of the size distribution of convective cloud clusters over West Africa and the Atlantic Ocean. *Mon. Wea. Rev.*, **121**, 37–49, https://doi.org/10.1175/1520-0493(1993)121<0037:DVAMBE>2.0.CO;2.

Mantripragada, R. S. S., C. J. Schreck, and A. Aiyyer, 2021: Energetics of interactions between African easterly waves and convectively coupled Kelvin waves. *Mon. Wea. Rev.*, **149**, 3821–3835, https://doi.org/10.1175/MWR-D-21-0003.1.

Martin, E. R., and C. Thorncroft, 2015: Representation of African easterly waves in CMIP5 models. *J. Climate*, **28**, 7702–7715, https://doi.org/10.1175/JCLI-D-15-0145.1.

McCrary, R. R., D. A. Randall, and C. Stan, 2014: Simulations of the West African monsoon with a superparameterized climate model. Part II: African easterly waves. *J. Climate*, **27**, 8323–8341, https://doi.org/10.1175/JCLI-D-13-00677.1.

Mekonnen, A., C. D. Thorncroft, and A. R. Aiyyer, 2006: Analysis of convection and its association with African easterly waves. *J. Climate*, **19**, 5405–5421, https://doi.org/10.1175/JCLI3920.1.

——, ——, ——, and G. N. Kiladis, 2008: Convectively coupled Kelvin waves over tropical Africa during the boreal summer: Structure and variability. *J. Climate*, **21**, 6649–6667, https://doi.org/10.1175/2008JCLI2008.1.

Molod, A., L. Takacs, M. Suarez, and J. Bacmeister, 2015: Development of the GEOS-5 atmospheric general circulation model: Evolution from MERRA to MERRA2. *Geosci. Model Dev.*, **8**, 1339–1356, https://doi.org/10.5194/gmd-8-1339-2015.

Moorthi, S., and M. J. Suarez, 1992: Relaxed Arakawa-Schubert. A parameterization of moist convection for general circulation models. *Mon. Wea. Rev.*, **120**, 978–1002, https://doi.org/10.1175/1520-0493(1992)120<0978:RASAPO>2.0.CO;2.

Mounier, F., G. N. Kiladis, and S. Janicot, 2007: Analysis of the dominant mode of convectively coupled Kelvin waves in the West African monsoon. *J. Climate*, **20**, 1487–1503, https://doi.org/10.1175/JCLI4059.1.

——, S. Janicot, and G. N. Kiladis, 2008: The West African monsoon dynamics. Part III: The quasi-biweekly zonal dipole. *J. Climate*, **21**, 1911–1928, https://doi.org/10.1175/2007JCLI1706.1.

Norquist, D. C., E. E. Recker, and R. J. Reed, 1977: The energetics of African wave disturbances as observed during phase III of GATE. *Mon. Wea. Rev.*, **105**, 334–342, https://doi.org/10.1175/1520-0493(1977)105<0334:TEOAWD>2.0.CO;2.

North, G. R., T. L. Bell, R. F. Cahalan, and F. J. Moeng, 1982: Sampling errors in the estimation of empirical orthogonal functions. *Mon. Wea. Rev.*, **110**, 699–706, https://doi.org/10.1175/1520-0493(1982)110<0699:SEITEO>2.0.CO;2.

Patricola, C. M., R. Saravanan, and P. Chang, 2018: The response of Atlantic tropical cyclones to suppression of African easterly waves. *Geophys. Res. Lett.*, **45**, 471–479, https://doi.org/10.1002/2017GL076081.

Pytharoulis, I., and C. Thorncroft, 1999: The low-level structure of African easterly waves in 1995. *Mon. Wea. Rev.*, **127**, 2266–2280, https://doi.org/10.1175/1520-0493(1999)127<2266:TLLSOA>2.0.CO;2.

Reed, R. J., A. Hollingsworth, W. A. Heckley, and F. Delsol, 1988: An evaluation of the performance of the ECMWF operational system in analyzing and forecasting easterly wave disturbances over Africa and the tropical Atlantic. *Mon. Wea. Rev.*, **116**, 824–865, https://doi.org/10.1175/1520-0493(1988)116<0824:AEOTPO>2.0.CO;2.

Rennick, M. A., 1976: The generation of African waves. *J. Atmos. Sci.*, **33**, 1955–1969, https://doi.org/10.1175/1520-0469(1976)033<1955:TGOAW>2.0.CO;2.

Russell, J. O. H., and A. Aiyyer, 2020: The potential vorticity structure and dynamics of African easterly waves. *J. Atmos. Sci.*, **77**, 871–890, https://doi.org/10.1175/JAS-D-19-0019.1.

——, ——, J. D. White, and W. Hannah, 2017: Revisiting the connection between African easterly waves and Atlantic tropical cyclogenesis. *Geophys. Res. Lett.*, **44**, 587–595, https://doi.org/10.1002/2016GL071236.

——, ——, and ——, 2020: African easterly wave dynamics in convection-permitting simulations: Rotational stratiform

instability as a conceptual model. *J. Adv. Model. Earth Syst.*, **12**, e2019MS001706, https://doi.org/10.1029/2019MS001706.

Schubert, W. H., P. E. Ciesielski, D. E. Stevens, and H.-C. Kuo, 1991: Potential vorticity modeling of the ITCZ and the Hadley circulation. *J. Atmos. Sci.*, **48**, 1493–1509, https://doi.org/10.1175/1520-0469(1991)048<1493:PVMOTI>2.0.CO;2.

Skinner, C. B., and N. S. Diffenbaugh, 2013: The contribution of African easterly waves to monsoon precipitation in the CMIP3 ensemble. *J. Geophys. Res. Atmos.*, **118**, 3590–3609, https://doi.org/10.1002/jgrd.50363.

Sultan, B., S. Janicot, and A. Diedhiou, 2003: The West African monsoon dynamics. Part I: Documentation of intraseasonal variability. *J. Climate*, **16**, 3389–3406, https://doi.org/10.1175/1520-0442(2003)016<3389:TWAMDP>2.0.CO;2.

Thorncroft, C. D., and B. J. Hoskins, 1994: An idealized study of African easterly waves. I: A linear view. *Quart. J. Roy. Meteor. Soc.*, **120**, 953–982, https://doi.org/10.1002/qj.49712051809.

——, and K. Hodges, 2001: African easterly wave variability and its relationship to Atlantic tropical cyclone activity. *J. Climate*, **14**, 1166–1179, https://doi.org/10.1175/1520-0442(2001)014<1166:AEWVAI>2.0.CO;2.

——, N. M. J. Hall, and G. N. Kiladis, 2008: Three-dimensional structure and dynamics of African easterly waves. Part III: Genesis. *J. Atmos. Sci.*, **65**, 3596–3607, https://doi.org/10.1175/2008JAS2575.1.

Tian, B., E. J. Fetzer, B. H. Kahn, J. Teixeira, E. Manning, and T. Hearty, 2013: Evaluating CMIP5 models using AIRS tropospheric air temperature and specific humidity climatology. *J. Geophys. Res. Atmos.*, **118**, 114–134, https://doi.org/10.1029/2012JD018607.

Tomassini, L., 2018: Mesoscale circulations and organized convection in African easterly waves. *J. Atmos. Sci.*, **75**, 4357–4381, https://doi.org/10.1175/JAS-D-18-0183.1.

——, D. J. Parker, A. Stirling, C. Bain, C. Senior, and S. Milton, 2017: The interaction between moist diabatic processes and the atmospheric circulation in African easterly wave propagation. *Quart. J. Roy. Meteor. Soc.*, **143**, 3207–3227, https://doi.org/10.1002/qj.3173.

Torn, R. D., 2010: Ensemble-based sensitivity analysis applied to African easterly waves. *Wea. Forecasting*, **25**, 61–78, https://doi.org/10.1175/2009WAF2222255.1.

Ullrich, P. A., and C. M. Zarzycki, 2017: TempestExtremes: A framework for scale-insensitive pointwise feature tracking on unstructured grids. *Geosci. Model Dev.*, **10**, 1069–1090, https://doi.org/10.5194/gmd-10-1069-2017.

——, ——, E. E. McClenny, M. C. Pinheiro, A. M. Stansfield, and K. A. Reed, 2021: TempestExtremes v2.1: A community framework for feature detection, tracking, and analysis in large datasets. *Geosci. Model Dev.*, **14**, 5023–5048, https://doi.org/10.5194/gmd-14-5023-2021.

Ventrice, M. J., C. D. Thorncroft, and P. E. Roundy, 2011: The Madden–Julian oscillation's influence on African easterly waves and downstream tropical cyclogenesis. *Mon. Wea. Rev.*, **139**, 2704–2722, https://doi.org/10.1175/MWR-D-10-05028.1.

——, ——, and C. J. Schreck, 2012a: Impacts of convectively coupled Kelvin waves on environmental conditions for Atlantic tropical cyclogenesis. *Mon. Wea. Rev.*, **140**, 2198–2214, https://doi.org/10.1175/MWR-D-11-00305.1.

——, ——, and M. A. Janiga, 2012b: Atlantic tropical cyclogenesis: A three-way interaction between an African easterly Wave, diurnally varying convection, and a convectively coupled atmospheric Kelvin wave. *Mon. Wea. Rev.*, **140**, 1108–1124, https://doi.org/10.1175/MWR-D-11-00122.1.

Yang, G.-Y., J. Methven, S. Woolnough, K. Hodges, and B. Hoskins, 2018: Linking African easterly wave activity with equatorial waves and the influence of Rossby waves from the Southern Hemisphere. *J. Atmos. Sci.*, **75**, 1783–1809, https://doi.org/10.1175/JAS-D-17-0184.1.

Zarzycki, C. M., and P. A. Ullrich, 2017: Assessing sensitivities in algorithmic detection of tropical cyclones in climate data. *Geophys. Res. Lett.*, **44**, 1141–1149, https://doi.org/10.1002/2016GL071606.

Zhao, H., X. Jiang, and L. Wu, 2016: Boreal summer synoptic-scale waves over the western North Pacific in multimodel simulations. *J. Climate*, **29**, 4487–4508, https://doi.org/10.1175/JCLI-D-15-0696.1.